


**Dynamics of turbulent plugs in a superfluid  $^4\text{He}$  channel counterflow**A. Pomyalov *Department of Chemical and Biological Physics, Weizmann Institute of Science, Rehovot, Israel*

(Received 13 February 2020; revised manuscript received 2 April 2020; accepted 2 April 2020; published 24 April 2020)

Quantum turbulence in superfluid  $^4\text{He}$  in narrow channels often takes the form of moving localized vortex tangles. Such tangles, called turbulent plugs, also serve as building blocks of quantum turbulence in wider channels. We report on a numerical study of various aspects of the dynamics and structure of turbulent plugs in a wide range of governing parameters. The unrestricted growth of the tangle in a long channel provides a unique view on a natural tangle structure including superfluid motion at many scales. We argue that the edges of the plugs propagate as turbulent fronts, following the advection-diffusion-reaction dynamics. This analysis shows that the dynamics of the two edges of the tangle have distinctly different nature. While bearing similarity to the dynamics of the patches of turbulent fluctuations during the transition to turbulence in the classical pipe flows, the superfluid turbulent fronts exhibit richer behavior. We provide an analytic solution of the equation of motion for the fronts that define their shape, velocities, and effective diffusivity, and analyze these parameters for various flow conditions.

DOI: [10.1103/PhysRevB.101.134515](https://doi.org/10.1103/PhysRevB.101.134515)**I. INTRODUCTION**

Quantum properties of liquid He become apparent [1–4] when it is cooled below critical temperature  $T_\lambda = 2.17$  K. A quantized part of fluid vorticity, an inviscid superfluid, forms a quantum ground state. A gas of thermal excitations represents a viscous normal fluid with continuous vorticity. The vorticity quantization results [5] in the creation of thin quantum vortex lines of fixed circulation. These lines form dense tangles that interact with the normal fluid via mutual friction force.

When placed in a channel with a temperature gradient, two components of the superfluid He flow in opposite directions. The superfluid flows towards the heater, while the normal fluid moves away from it. Such a setting, called thermal counterflow, has been long used to study [6–8] properties of superfluid  $^4\text{He}$  components and their interaction. Early experiments on the thermal counterflow in  $^4\text{He}$  in narrow channels found a wide variety of scenarios of the vortex tangle dynamics [6,8–12]. Propagating turbulent fronts and localized vortex tangles, or turbulent plugs were observed in long thin glass and metal capillaries [8–10]. Depending on conditions, these plugs were either stationary, moving in one direction or expanding both toward and away from the heater.

The stationary, almost homogeneous tangles, filling the whole channel, were found in relatively wide channels [6,7,11,12]. In this case, the local variations of the vortex line density (VLD) buildup towards the stationary regime were considered as transient effects [11] and most of the attention turned to studies of the steady-state properties with VLD being the main parameter of the system.

Derivation of a set of closed equations for the description of the quantum vortex tangle dynamics and statistics using only its macroscopic characteristics have been an ultimate goal since early days of superfluid  $^4\text{He}$  studies. The Vinen's equation [6] for the time evolution of the vortex line density  $\mathcal{L}$  in a homogeneous tangle served as a basis of most theoretical

considerations for decades (see, for example, Refs. [13–15]). A microscopic theory by Schwarz [16] introduced additional structural properties of the tangle, such as root-mean-square curvature and various anisotropy parameters, as important ingredients of the theory [17–19]. As was pointed out by Schwarz, the arguments leading to these equations for  $\mathcal{L}$  apply only to the average time-dependent behavior near the steady state, although they are very often used in other situations.

For a moving tangle, a number of theories [13,15,20] predicted that the plug motion is defined by drift as a whole with a constant velocity and a diffusionlike spreading. It was commonly assumed that the fully developed homogeneous tangle is expanding into the laminar superfluid, having well-defined properties, the same as for the stationary homogeneous tangle. No direct experimental or numerical evidence, supporting these assumptions, was found so far. The only numerical study of such a moving turbulent plug by Schwarz [21] was carried out within an approximation that ignores nonlocal interactions between vortex lines and was fully focused on the conditions that allow sustaining the quantum turbulence.

Recent advances in the experimental techniques, including flow visualization [22–24], as well as increased computing power, renewed the interest to the spatial inhomogeneity due to presence of channel walls [19,25–31] and spatially resolved investigations of the transient behavior in the thermal counterflow [32]. The latter work showed that the vortex tangle that eventually fills the whole channel, grows starting from a number of remnant vortex rings. These rings first form separate localized turbulent plugs, which later merge. Remarkably, the structural properties of the large-scale tangle become homogeneous soon after the merger, while the vortex line density distribution remain inhomogeneous much longer, as reflected by very different VLD build-up patterns at different locations in the channel.

There is a strong similarity between the localized vortex tangle development in the superfluid helium and the

formation of the localized turbulent structures (so-called puffs and slugs) in the classical pipe and duct flows [33–37] during the transition of the laminar flow to the turbulent regime. In the classical flow, the patches of the turbulent velocity fluctuations are carried by the laminar flow. However, due to the strong temperature dependence of the  $^4\text{He}$  material properties and the efficient energy exchange between two fluid components, the dynamics of the turbulent plugs in the superfluid helium is expected to be more complex, even in the mechanically driven superfluid helium in which both fluid components move in the same direction.

In this paper, we study the dynamical and structural properties of localized turbulent plugs formed in the superfluid  $^4\text{He}$  counterflow in the wide range of flow conditions. Unlike previous simulations of the thermal counterflow in the channel, here the vortex tangle development in the streamwise direction is undisturbed by artificial self-interactions, caused by periodic boundary conditions. Such conditions are routinely used to ensure the quick creation of a dense tangle that is homogeneous in the streamwise direction. Although convenient, this approach does not allow us to study the natural structure of the tangle and the local influence of the mean superfluid velocity on the vortex lines motion.

The paper is organized as follows. In Sec. II, we consider the vortex tangle motion as a whole and the spatial distribution of the vortex line density in the developing tangle. We start by introducing in Sec. II A important notions and parameters of the thermal counterflow in superfluid  $^4\text{He}$ . Then we describe the numerical setup (Sec. II B) and the chosen ways for the characterization of the developing vortex tangle in the channel (Sec. II C). Next, we consider the spatiotemporal evolution of the tangle vortex line density (Sec. II D), while peculiarities of the transient processes are discussed in Sec. II E. The large-scale superfluid motion, created inside the vortex tangle, is described in Sec. II F. In Sec. II G, we focus on the structural properties of the developed tangle. Section III is devoted to the study of the VLD front dynamics and structure. First, we overview important information from the turbulent front propagation studies, relevant for the current work (Sec. III A). Next, we derive an equation of motion for VLD, that describes the evolution of the tangle edges, or fronts (Sec. III B), show that the two tangle fronts have different nonlinearity types (Sec. III C), consider the closure for the nonlinear term (Sec. III D), and solve the equation of front motion analytically for the front shape (Sec. III E). Then we discuss the parameters, that describe the front propagation: the front velocities (Sec. III F) and the effective diffusivity (Sec. III G). In Sec. IV, we summarize our findings. Additional information may be found in Appendixes. Appendix A provides a thematically organized guide to the main notations used in the paper. The procedures for the calculation of various profiles and the front shapes are described in Appendixes B and C. The detailed analysis of various contributions to the equation of motion for VLD is given in Appendix D.

## II. DYNAMICS AND STRUCTURE OF TURBULENT PLUGS

### A. The counterflow turbulence in the channel

As already mentioned, at temperatures below  $T_\lambda = 2.7\text{ K}$ , liquid  $^4\text{He}$  become a superfluid. In this state, the superfluid

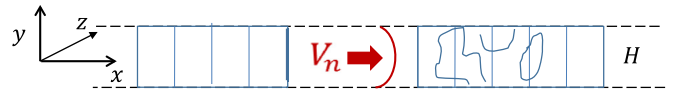


FIG. 1. Numerical setup. The simulations are set up in a long planar channel of a width  $H$ . The normal-fluid velocity is oriented towards positive  $x$  direction.

He of the density  $\rho$  is often described [1,3] in the framework of the two-fluid model as an interpenetrating mixture of a normal fluid with the density  $\rho_n$  and a superfluid component of the density  $\rho_s$ , such that  $\rho_s + \rho_n = \rho$  and the component contributions  $\rho_s, \rho_n$  are strongly temperature dependent [38].

The normal-fluid component has low viscosity and continuous vorticity, while the superfluid is inviscid and its vorticity is constrained to vortex-line singularities of core radius  $a_0 \approx 10^{-8}\text{ cm}$  with fixed circulation  $\kappa = h/M \approx 10^{-3}\text{ cm}^2/\text{s}$ , where  $h$  is Planck's constant and  $M$  is the mass of the  $^4\text{He}$  atom. The two components are coupled by the mutual friction force. Under the influence of the temperature gradient applied along the channel, the normal fluid is moving away from the heater with a mean velocity  $V_n$ . At the same time, the superfluid is moving towards the heater with the mean velocity  $V_s$ , creating a relative, or a counterflow, velocity  $V_{ns} = V_n - V_s$ , proportional to the applied heat flux. The chaotic tangle of vortex lines is then generated from pre-existing remnant vortex loops due to the coupling by temperature-dependent mutual friction force. The governing parameters that define the dynamics and the structure of the tangle are, therefore, the counterflow velocity and the temperature, while the geometric constraints, such as channel dimensions, influence the inhomogeneity of the vortex tangle.

### B. Numerical setup

The simulations were set up in a long planar channel of a width  $H$  (see Fig. 1). To describe dynamics of the vortex lines we use the vortex filament method [16,39,40] for the channel flow [26,29,32]. The vortex lines are parameterized by curves  $s(\xi, t)$  and discretized in a set of points with the resolution  $\Delta\xi = 0.001\text{ cm}$ . In this way, a local coordinate system is associated with each vortex line point  $s(\xi)$ , such that  $s' \equiv ds/d\xi$  is the unit vector denoting the local direction of the vortex line,  $s'' \equiv d^2s/d\xi^2$  is the local curvature vector, and  $(s' \times s'')$  is the local binormal vector. Here primes denote differentiation with respect to the instantaneous arc length  $\xi$ . The equation of motion for such a line point [16] is

$$\frac{ds(\xi, t)}{dt} = \mathbf{V}_{\text{drift}}(s, t) = \mathbf{V}_s(s, t) + \mathbf{V}_{\text{mf}}(s, t),$$

$$\mathbf{V}_{\text{mf}}(s, t) = (\alpha - \alpha' s' \times s'') \mathbf{s}' \times \mathbf{V}_{\text{ns}}(s, t), \quad (1)$$

where  $\alpha, \tilde{\alpha}$  are the temperature-dependent mutual friction parameters [38]. The right-hand side (RHS) of Eq. (1) represents the drift velocity of the tangle  $\mathbf{V}_{\text{drift}}$ . The superfluid velocity

$$\mathbf{V}_s = \mathbf{V}_{\text{BS}} + \mathbf{V}_s^0, \quad (2)$$

$$\mathbf{V}_{\text{BS}}(s, t) = \frac{\kappa}{4\pi} \int_{\Omega} \frac{\mathbf{s} - \mathbf{s}_1}{|\mathbf{s} - \mathbf{s}_1|^3} \times d\mathbf{s}_1 = \mathbf{V}_{\text{loc}} + \mathbf{V}_{\text{nl}}, \quad (3)$$

TABLE I. Material properties [38] of  $^4\text{He}$  used in the simulations: the ratio of the partial densities  $\rho_n/\rho_s$  and the mutual friction parameters  $\alpha$ ,  $\alpha'$ .

$T$ , K	1.3	1.65	1.9
$\rho_n/\rho_s$	0.047	0.239	0.723
$\alpha$	0.034	0.11	0.206
$\alpha'$	0.0138	0.0144	0.0083

accounts for the tangle contribution  $\mathbf{V}_{\text{BS}}(s, t)$  and the mean superfluid velocity  $\mathbf{V}_s^0$  that is defined by the counterflow condition of zero mass flux. In its turn,  $\mathbf{V}_{\text{BS}}$  may be further divided into the local part, produced by the scales up to local radius of curvature  $R = 1/|s''|$ ,  $\mathbf{V}_{\text{loc}} = \beta(s' \times s'')$ ,  $\beta = (\kappa/4\pi) \ln(R/a_0)$  and the nonlocal velocity  $\mathbf{V}_{\text{nl}}$  which is produced by the rest of the tangle  $\Omega$ . The mutual friction part  $\mathbf{V}_{\text{mf}}(s, t)$  describes the interaction with the normal fluid via counterflow velocity  $\mathbf{V}_{\text{ns}}(s, t) = \mathbf{V}_n - \mathbf{V}_s(s, t)$ . The material parameters of  $^4\text{He}$ , used in the simulations, are listed in Table I. The time resolution for the vortex line point is set by the fourth-order Runge-Kutta stability criterion.

To generate the counterflow, we use two time-independent prescribed wall-normal profiles of the streamwise projection of the normal-fluid velocity  $V_n^x(y)$ , shown in Fig. 2. The parabolic profile corresponds to the laminar normal-fluid velocity. It was observed experimentally at low heat fluxes. At larger heat fluxes, when the normal fluid loses its stability but not yet become fully turbulent, its profile flattens [41]. Similar flattening of the normal-fluid velocity profile was found in simulations with a two-way coupling of the fluid components [42,43]. Although such a fully coupled dynamics gives the most reliable description of the superfluid  $^4\text{He}$ , it is still computationally prohibitive for sufficiently large systems and long propagation times. Therefore we ignore the back-influence of the superfluid component on the normal fluid and model the expected normal-fluid velocity flattening by

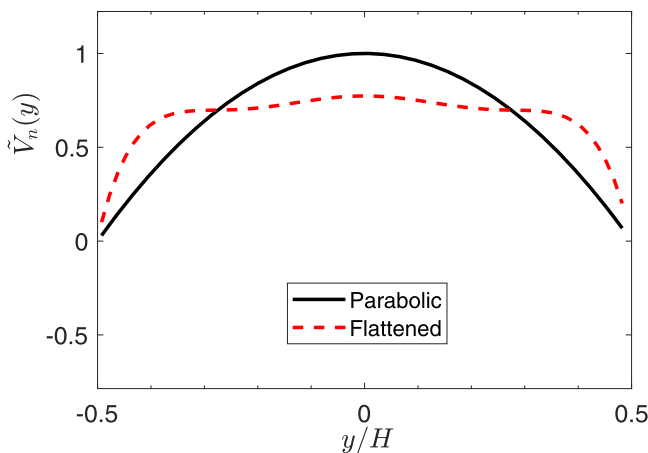


FIG. 2. Normal-fluid velocity profiles normalized by the mean value  $\tilde{V}_n = V_n/\langle V_n \rangle$ . The shape of the flattened profile is defined by a combination of six Legendre polynomials, such that it has the same  $\langle V_n \rangle$  as the corresponding parabolic profile.

imposing the corresponding time-independent profile (dashed line in Fig. 2).

The mean superfluid velocity  $V_s^0$  is dynamically defined by the zero-mass-flux condition

$$\rho_n \langle V_n \rangle_v + \rho_s \langle V_s^0 \rangle_v = 0, \quad (4)$$

where  $\langle \dots \rangle_v$  denotes global volume averaging and  $V_s^0$  includes a contribution of the superfluid velocity induced by the vortex tangle, calculated on a dense grid. This contribution, although small, is not negligible and grows with the development of the spatially inhomogeneous tangle.

To mimic solid walls in the wall-normal direction, the boundary conditions on the wall are  $s'(\pm H/2) = (0, \pm 1, 0)$  and  $V_s^y(\pm H/2) = 0$ . In the spanwise direction, periodic conditions were used. To ensure the free evolution of the developing tangle, we use open conditions in the streamwise direction. In this way, the properties of the tangle edges, moving as fronts, as well as the natural structure of the tangle bulk, can be studied.

The vortex tangles at all conditions were initiated using the same set of eight vortex loops of similar sizes  $R_0 \ll H$  and different orientations. The loops were placed at a particular streamwise location, four circular loops in the bulk and four half-circular loops at the walls. The difference in the dynamics of these tangles, therefore, originates from the flow conditions only, allowing comparison. We have verified that the particular choice of the initial conditions influence only the very early stages of the vortex dynamics before the three-dimensional tangle is formed. This stage usually lasts the first 1–2 seconds of evolution. After that, the structure and the dynamics of the tangles are defined only by the temperature and the flow conditions.

The tangle dynamics was studied at three temperatures  $T = 1.3, 1.65, \text{ and } 1.9$  K. Other simulation parameters include various normal-fluid velocities. In most simulations, the parabolic profile for  $V_n$  and a narrow channel width  $H = 0.1$  cm was used. At each temperature, one case was chosen for simulations with wider channels and with flattened normal-fluid velocity profile (the same  $\langle V_n \rangle$  as for the corresponding parabolic profile). The simulation parameters are listed in Table II, columns 2–7. In all simulations, the size of the channel in the  $z$  direction was always equal to  $H$ . Despite the periodic boundary conditions in the spanwise direction, the interaction between the vortex lines and their images is an important factor in the current setting. The study of the influence of the slit aspect ratio on the tangle dynamics is beyond the scope of this paper. The tangle evolution was followed until a well-developed bulk tangle was formed, such that the final length of the tangle is about 4–8  $H$ . The actual final time of evolution  $t_f$  varies for different conditions.

### C. Characterization of the tangle

To characterize the developing tangle, we calculate the time-dependent two-dimensional (2D)  $(x, y)$ -spatial distribution of tangle properties, averaged over spanwise  $z$  direction, at equispaced time moments. To this end, we define a fixed grid with a resolution  $\Delta x = 0.011$  cm and  $\Delta y = 0.0015$  cm. The 2D maps of the tangle properties are calculated by integration [16] over parts of the tangle  $\Omega'$  that fall into a grid

TABLE II. Parameters of simulations by columns: (1) run number, (2) temperature; (3) type of  $V_n$  profile: P denote parabolic profile, F denote for flattened profile; (4) channel width; (5) centerline velocity  $U_c$ ; and (6) mean normal-fluid velocity  $\langle V_n \rangle$ . For the parabolic profile,  $\langle V_n \rangle = 2/3 U_c$ ; (7) mean counterflow velocity  $V_{ns}^0 = \langle V_n \rangle_y (1 + \rho_n / \rho_s)$ ; (8) bulk VLD in the core of the channel  $\mathcal{L}_0^{\text{core}}$ ; and (9) bulk VLD near the walls  $\mathcal{L}_0^{\text{wall}}$ . The error bars for  $\mathcal{L}_0^j$  account for the standard deviation from the mean values.

1	2	3	4	5	6	7	8	9
Run	$T$ K	Type	$H$ cm	$U_c$ cm/s	$\langle V_n \rangle$ cm/s	$V_{ns}^0$ cm/s	$\mathcal{L}_0^{\text{core}} \times 10^{-4}$ $\text{cm}^{-2}$	$\mathcal{L}_0^{\text{wall}} \times 10^{-4}$ $\text{cm}^{-2}$
1	1.3	P	0.1	2	1.66	1.4	$0.37 \pm 0.03$	$0.6 \pm 0.1$
2	1.3	P	0.1	3	2	2.11	$0.95 \pm 0.05$	$1.5 \pm 0.4$
3	1.3	P	0.1	4	2.66	2.84	$2.20 \pm 0.06$	$3.2 \pm 0.8$
4	1.3	F	0.1	—	2	2.11	$1.3 \pm 0.3$	$1.5 \pm 0.2$
5	1.3	P	0.15	3	2	2.12	$1.0 \pm 0.2$	$1.4 \pm 0.4$
6	1.3	P	0.2	3	2	2.11	$7.1 \pm 0.2$	$8.2 \pm 0.2$
7	1.65	P	0.1	1.5	1	1.22	$0.86 \pm 0.02$	$1.3 \pm 0.3$
8	1.65	P	0.1	2	1.66	1.63	$1.84 \pm 0.03$	$2.5 \pm 0.5$
9	1.65	F	0.1	—	1	1.2	$1.29 \pm 0.02$	$1.4 \pm 0.2$
10	1.9	P	0.1	1	0.66	1.19	$1.87 \pm 0.02$	$2.1 \pm 0.3$
11	1.9	P	0.1	1.2	0.8	1.42	$2.92 \pm 0.03$	$3.2 \pm 0.3$
12	1.9	P	0.1	1.5	1	1.36	$4.6 \pm 0.1$	$4.8 \pm 0.6$
13	1.9	F	0.1	—	0.66	1.17	$2.55 \pm 0.05$	$2.5 \pm 0.6$
14	1.9	P	0.15	1	0.66	1.18	$1.82 \pm 0.04$	$2.0 \pm 0.2$
15	1.9	P	0.2	1	0.66	1.17	$1.84 \pm 0.06$	$1.7 \pm 0.2$

cell  $V' = \Delta x \times \Delta y \times H$ . In such a way we obtain the vortex line density  $\mathcal{L}$ , the curvature of the vortex lines  $\varkappa \equiv |s''|$ , the mean square curvature  $\langle \varkappa^2 \rangle$ , the ratio  $c_2^2 = \langle \varkappa^2 \rangle / \mathcal{L}$ , the local binormal  $\mathbf{I}_\ell = \langle \mathbf{s}' \times \mathbf{s}'' \rangle$  and its anisotropy index  $\mathbf{I}_\ell^\dagger = \langle \mathbf{s}' \times \mathbf{s}'' \rangle / (|s''|)$ , the contributions to the tangle drift velocity, as defined by the right-hand side of (1) and various terms of the balance equation, defined by Eq. (17). In the above definitions, the arguments  $(x, y, t)$  were omitted for clarity. To compare the results for different flow conditions, we use dimensionless quantities, normalized using the mean counterflow velocity calculated from the zero-mass-flux condition  $V_{ns}^0 = \langle V_n \rangle_y (1 + \rho_n / \rho_s)$  and the circulation quantum  $\kappa$ . The procedures for the calculation of various profiles are described in Appendix B.

To measure the velocity of front propagation, it is customary to choose a threshold value of propagating quantity and to follow the change of its position. To avoid inevitable freedom in the choice of the threshold value  $\mathcal{L}$ , we use here a different approach. Instead of following a single threshold value, we find the velocity that allows collapsing the whole edge of the tangle to a single shape. It turned out that such an approach gives a very robust measurement of the velocity, allowing simultaneously to study the front shape. The speeds of both VLD fronts were measured over the time interval when the tangle bulk is formed and the fronts do not change their shape during propagation. The details on the procedure are described in Appendix C. The values of bulk VLD in the channel core and near the walls are listed in Table II, columns 8 and 9. The error bars here and in Figs. 15 and 18, correspond to the standard deviation around the mean values.

#### D. Evolution of VLD

The examples of the evolution of the vortex line density at low and high temperatures are shown in Fig. 3. These examples illustrate the main difference in the flow conditions that crucially affect the tangle dynamics. The vortex tangle is advected by the superfluid velocity field. At low  $T$ , the mean superfluid velocity  $V_s^0$  is weak due to a small fraction of the normal fluid [cf. Eq. (4)]. The tangle dynamics is governed mostly by the tangle-induced velocity and a net tangle displacement is negligible, as is illustrated in Fig. 3(b). On the other hand, at high temperature,  $V_s^0$  and  $V_n$  are comparable and the tangle is flushed along the channel by the mean superfluid velocity, see Fig. 3(d). Under all conditions, the vortex tangle develops as a moving turbulent plug. At  $T = 1.9$  K, the initial vortex rings are at first separated into at least two groups that grow into independent turbulent plugs that later merge. The developing tangles are inhomogeneous in both the streamwise and wall-normal directions, as is illustrated by snapshots of 2D VLD distributions at various time moments in Figs. 3(a) and 3(c).

The VLD is higher near the walls, similar to the steady-state tangles with the parabolic profile of the driving normal-fluid velocity, obtained under periodic streamwise conditions [25–27,29,42]. Two edges of the tangle are different: a narrow and sharp edge is formed in the direction of  $V_n$  and a wide and less steep edge in the direction of  $V_s$ . As we show later, these edges move with constant velocities and without changing their shape. We, therefore, label them as a hot front (moving the direction of normal-fluid velocity away from the heater) and a cold front (moving in the direction of mean superfluid velocity toward the heater). In the further analysis, we distinguish a near-wall and a core regions in the wall-normal direction and a bulk and the fronts regions in the streamwise direction, see Fig. 22.

To characterize the distribution of VLD along and across the tangle, we plot its streamwise profiles in Fig. 4 and wall-normal profiles in Fig. 5. The dynamics of VLD, obtained with the parabolic normal-fluid velocity at various values of  $U_c$ , differ mostly by the duration of transient behavior in the tangle core and the mean value of VLD in the bulk of the tangle.

In Fig. 4, we compare the streamwise VLD profiles for the parabolic and for the flattened normal-fluid profiles at similar  $t_f$ . At low  $T = 1.3$  K [Figs. 4(a) and 4(b)], the vortex line density at the walls in both cases reached similar values, while the core region for the parabolic  $V_n(y)$ , shown in Fig. 4(a), is still not fully developed (see Sec. II E for details). The length of the tangle in both cases is about  $3.5 H$ . The edges of the tangles reached similar streamwise positions indicating similar fronts velocities. At high  $T = 1.9$  K, Figs. 4(c) and 4(d),  $\mathcal{L}(x)$  for both  $V_n$  profiles is almost homogeneous in the tangle bulk. Here, however, the hot edge moved faster for the flattened  $V_n(y)$ , leading to a shorter plug. The mean VLD in the bulk, in this case, is about 20% higher than for the parabolic profile.

To compare the wall-normal VLD profiles for various flow conditions, we plot in Fig. 5 a dimensionless VLD  $\mathcal{L}^\dagger(y) = \mathcal{L}(y)\kappa^2 / (V_{ns}^0)^2$ . Here we compare  $\mathcal{L}^\dagger(y)$  for the parabolic and flattened  $V_n(y)$  for the narrow channel  $H = 0.1$  cm in panels (a) and (c) and for various channel widths, using the parabolic

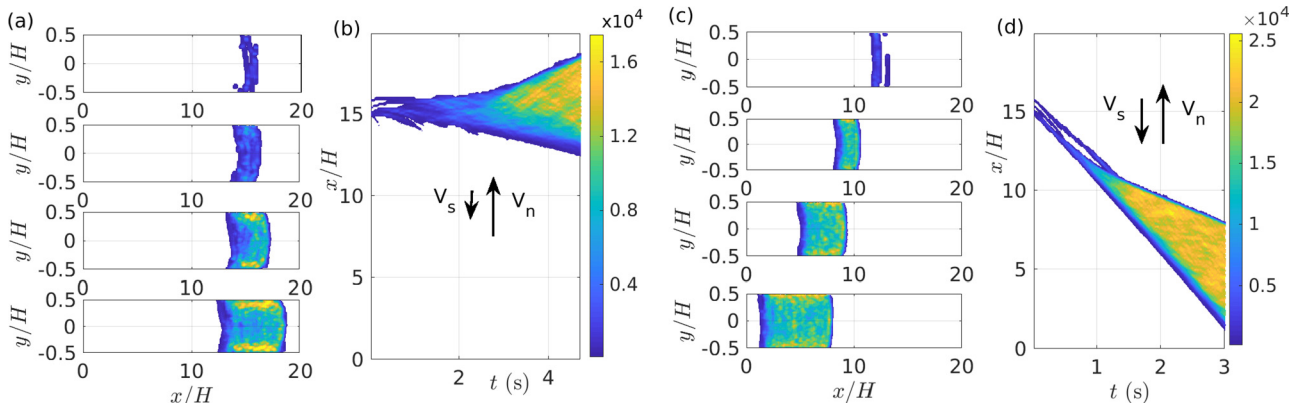


FIG. 3. VLD evolution. [(a) and (b)]  $T = 1.3$  K,  $U_c = 3$  cm/c. [(c) and (d)]  $T = 1.9$  K,  $U_c = 1$  cm/c. (a) and (c) show  $\mathcal{L}(x, y)$  distribution at  $t = 0.2$  s,  $t_f/2$ ,  $3t_f/4$ , and  $t_f$  with the top snapshot corresponding to the early stages of the dynamics and the bottom snapshot corresponding to  $t_f$ . (b) and (d) show the time evolution of VLD averaged over  $y$  direction  $\mathcal{L}(x, t)$ . Both cases correspond to the parabolic profile of  $V_n$  and the channel width  $H = 0.1$  cm. The values of  $\mathcal{L}$  are color-coded as shown by color bars in (b) and (d).

normal-fluid velocity profile with the same  $U_c$ , in panels (b) and (d).

First of all, we note that the wall-normal profiles  $\mathcal{L}(y)$  are consistent with the profiles obtained in the steady-state tangles [26,29] with the VLD peaking near the wall at about the intervortex distance. The flattened profiles [thin red lines in (a) and (c)] have larger VLD values in the tangle core. The  $\mathcal{L}^\dagger(y)$  near the walls is higher for the parabolic  $V_n$  profile at  $T = 1.3$  K and similar for both profiles at  $T = 1.9$  K. At both temperatures, VLD for the flattened  $V_n(y)$  is homogeneous not only over the core region but also over a large part of the near-wall region, especially at  $T = 1.9$  K. A similar effect of flattening of VLD profile is observed in wider channels for the parabolic  $V_n(y)$ , indicating that the increase of VLD near the walls is indeed related to the boundary effect. These profiles are compared in Figs. 5(b) and 5(d). At both temperatures, the tangles for widest channels  $H = 0.2$  cm are not yet fully developed, although in a different way: at low  $T$  the VLD just did not reach the expected values, while at high  $T$  the

tangle is formed by merging of two independent vortex plugs [similar to shown in Fig. 3(d)]. The resulting streamwise inhomogeneity does not allow to properly resolve the near-wall region in the profiles calculated over narrow tangle bulk. However, it can be clearly seen that, as the channel become wider, the range of nearly flat VLD distribution extends from the core to the near-wall region, in a way similar to the flow, generated by the flattened  $V_n(y)$  profile. Comparing the VLD profiles for  $H = 0.1$  and 0.15 cm, we find that at low temperature the VLD is peaking stronger near the walls, while at high  $T$  the near-wall VLD is similar for both channel width. The normalized positions of the peaks do not change with the channel width, meaning that the peaks appear further from the wall for wider channels.

To rationalize these observations we plot in Fig. 6 the profiles of various velocities, normalized by the counterflow velocity  $V^\dagger = V/V_{ns}^0$ . We start with the streamwise component of the superfluid velocity  $V_s^x(y) = V_s^0 + V_{BS}^x$ . Near the walls  $V_s < 0$  for all flow conditions and close to  $V_s^0$ . The main

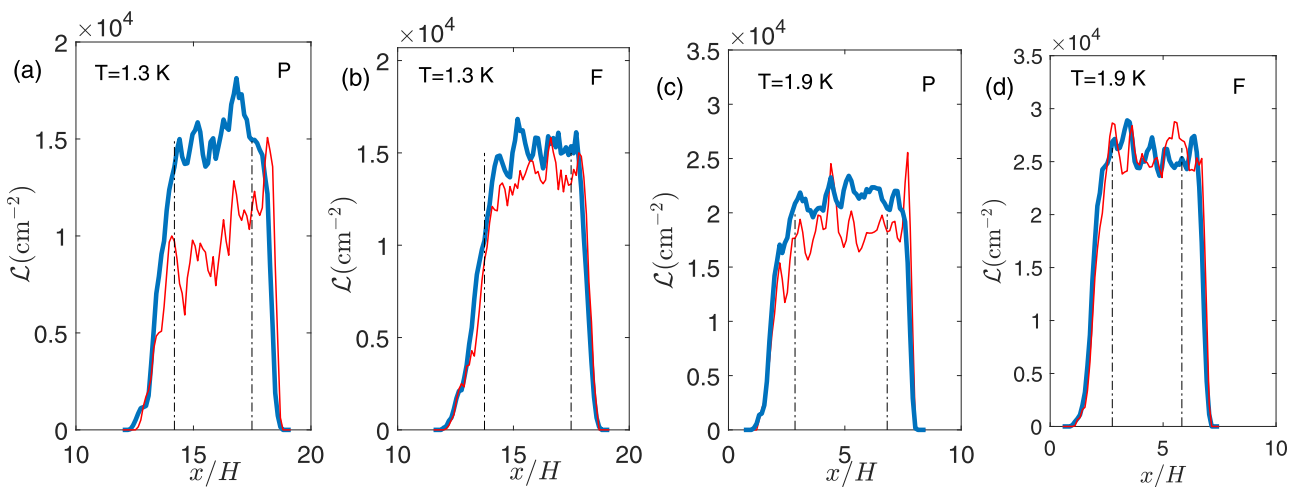


FIG. 4. The streamwise VLD profiles  $\mathcal{L}(x)$  for  $T = 1.3$  K [(a) and (b)] and  $T = 1.9$  K [(c) and (d)]. The parabolic profile of  $V_n$  (P) was used in (a) [ $U_c = 3$  cm/s] and (c) [ $U_c = 1$  cm/s]. In (b) and (d), the flattened  $V_n$  profiles (F) were used, with the same ( $V_n$ ) as in (a) and (c), respectively. The profiles for the walls region are shown by thick blue lines and for the core region by thin red lines. Vertical dot-dashed lines denote the edges of the bulk region. The channel width is  $H = 0.1$  cm and  $t = t_f$ .

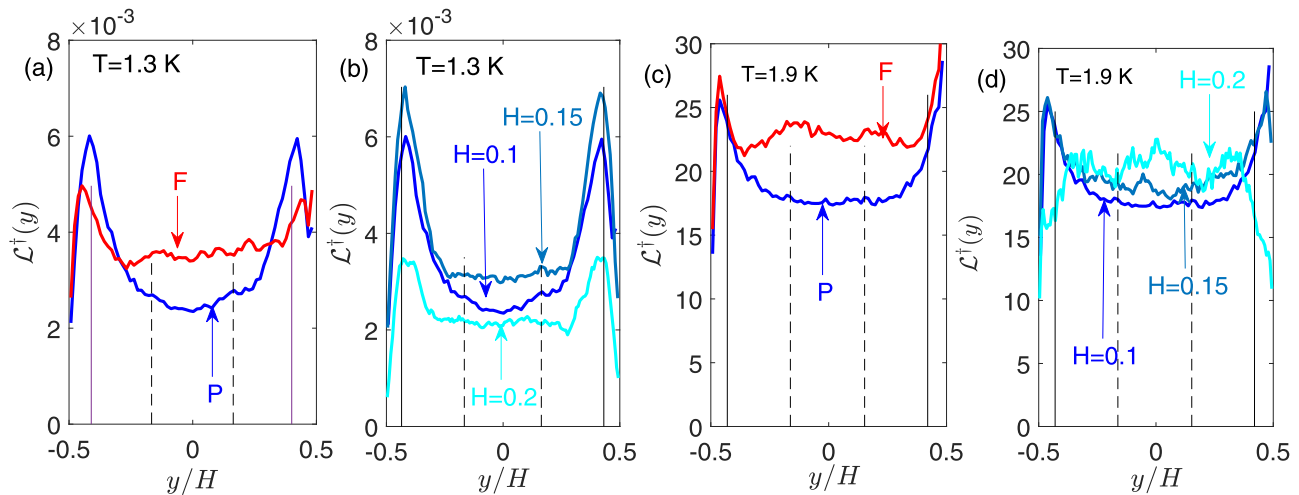


FIG. 5. The wall-normal profiles of dimensionless VLD profiles  $\mathcal{L}^\dagger(y)$  for  $T = 1.3$  K [(a) and (b)] and  $T = 1.9$  K [(c) and (d)]. (a) and (c) compare the  $\mathcal{L}^\dagger(y)$  profiles for the parabolic (P) and the flattened (F)  $V_n$  profiles at  $H = 0.1$  cm. (b) and (d) compare the  $\mathcal{L}^\dagger(y)$  profiles for the parabolic  $V_n$  and different channel widths labeled in the figures by their values. All profiles at  $T = 1.3$  K correspond to  $U_c = 3$  cm/s, the profiles at  $T = 1.9$  K correspond to  $U_c = 1$  cm/s. Here, and in Figs. 6–8, dashed vertical lines denote edges of the channel core. Thin solid black lines are placed at the intervortex distance from the walls. In each panel only one intervortex distance is shown to avoid clutter.

difference between the superfluid velocity behavior at low  $T$  [panels (a) and (b)] and at high  $T$  [panels (c) and (d)] is in the channel core, where at  $T = 1.3$  K  $V_s > 0$ , while at  $T = 1.9$  K,  $V_s < 0$ . As a result, at low  $T$ , the value of  $V_{ns}$  is smaller than  $U_c$ , while at high  $T$ ,  $V_{ns}$  is larger than  $V_n$  everywhere in the channel and homogeneous across the core even for the parabolic  $V_n$  profile. Furthermore, as is shown in Fig. 7(a), the shape of  $V_{ns}(y)$  remains almost unchanged with increasing  $H$  at low temperature while becoming flat over an increasingly larger part of the channel as the channel become wider at high  $T$ , Fig. 7(b). Since the tangle dynamics is defined by  $V_{ns}$  according to Eq. (1), such behavior may explain the tendency for a more homogeneous VLD distribution in wider channels at high  $T$  than at low temperature.

The superfluid velocity plays an additional role in the dynamics. It is usually assumed that the overall tangle motion is defined by the superfluid velocity  $V_s^0$ . However, as is shown in Figs. 3(b) and 3(d), the fronts of the tangle may both move in the direction of  $V_s^0$ , or only cold front moves with  $V_s^0$ , while the hot front moves in the opposite direction. It is natural to associate the direction of the cold front motion with the direction of the superfluid velocity  $V_s$  near the walls, while the direction of the hot front motion with the direction of  $V_s$  in the core of the channel. Such an assumption is further supported in Fig. 8, where we plot the  $V_s$  and  $V_{ns}$  velocities for the intermediate  $T = 1.65$  K, and Fig. 9, where we plot the evolution of the corresponding  $\mathcal{L}(x, t)$ . Here the superfluid velocity in the channel core is close to zero and the behavior of the hot front is very sensitive to the flow conditions. The

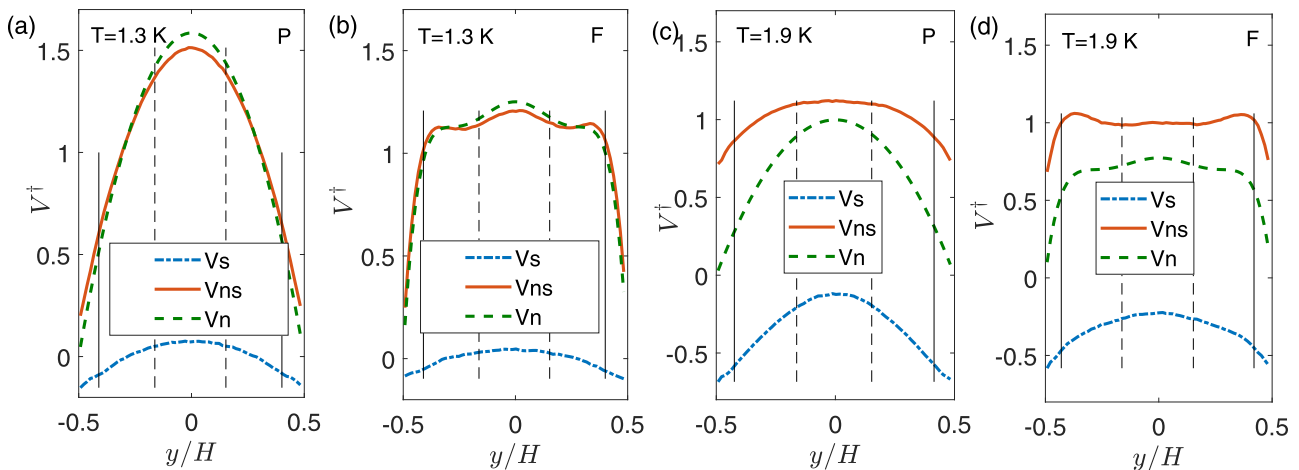


FIG. 6. The wall-normal profiles of normalized velocities  $V_s^{\dagger}$ ,  $V_n^{\dagger}$ , and  $V_{ns}^{\dagger}$ . (a) and (b) compare the profiles for the parabolic (P) and the flattened  $V_n$  (F) profiles for  $T = 1.3$  K,  $U_c = 3$  cm/c, (c) and (d) compare the velocity profiles for  $T = 1.9$  K and  $U_c = 1$  cm/c. The channel width is  $H = 0.1$  cm. Green dashed lines denote the driving  $V_n(y)$  profiles, blue dot-dashed lines denote the full streamwise superfluid velocity  $V_s^\dagger(y) = V_s^0 + V_{BS}^\dagger(y)$ , solid red lines denote the profiles of the counterflow velocity  $V_{ns}^\dagger(y) = V_n(y) - V_s^\dagger(y)$ .

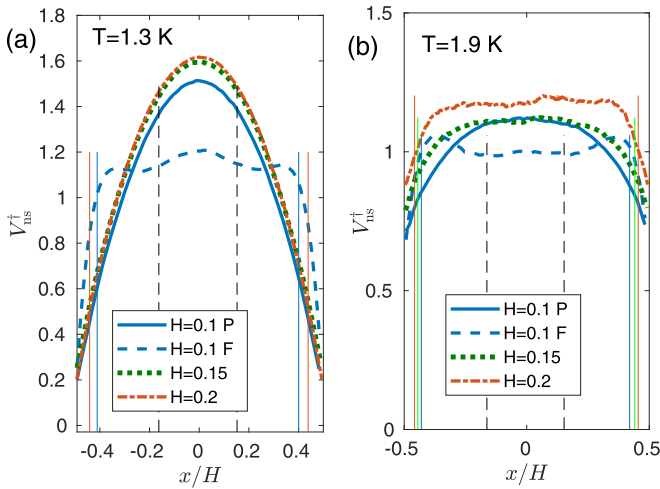


FIG. 7. The wall-normal profiles of normalized  $V_{ns}^\dagger$  profiles for the parabolic  $V_n$  at various channel widths and for the flattened  $V_n$  (dashed lines) profiles for (a)  $T = 1.3$  and (b)  $1.9$  K. The solid lines correspond to  $H = 0.1$  cm, dotted lines for  $H = 0.15$  cm, dot-dashed lines correspond to  $H = 0.2$  cm. Thin vertical lines are placed at the intervortex distance from the walls, their colors match the color of the corresponding velocity profiles.

superfluid velocity for the flattened  $V_n$  profile, shown in Fig. 8 as the blue dashed line, is negligible at the center of the channel and the corresponding hot VLD front [Fig. 9(c)] is stationary. The hot VLD front in the flow generated by the parabolic  $V_n(y)$  with  $U_c = 1.5$  cm/s, for which  $V_s(0) \lesssim 0$ , has hardly settled [Fig. 9(a)], despite relatively long propagation time. On the other hand, at larger  $U_c = 2$  cm/s, we clearly see in Fig. 8(b) the hot front moving opposite to the direction of  $V_s^0$ . The cold fronts under all conditions move with  $V_s^0$ , although the front speeds differ. Here, the cold front speed for the flattened  $V_n$  profile is smaller than for the corresponding parabolic  $V_n(y)$ , consistently with a smaller value of  $V_s$  at the walls. The fronts speeds are *not equal* to  $V_s$  at the wall or in the core, although they are clearly related.

### E. Transient dynamics

In this section, we consider the transient dynamics of the growing turbulent plugs for different conditions. Here we

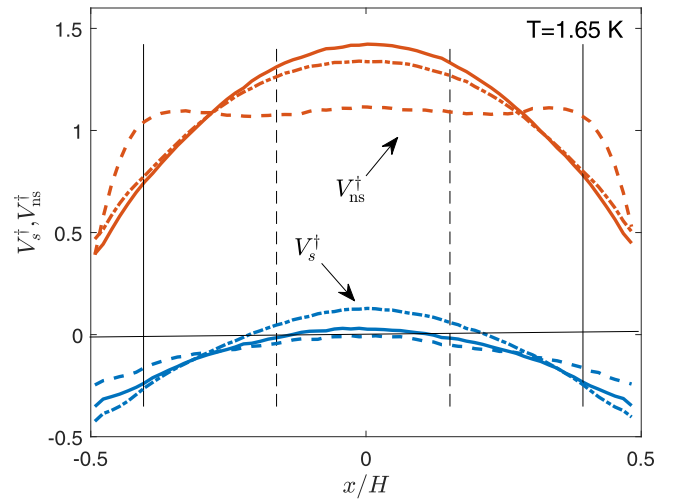


FIG. 8. The wall-normal profiles of normalized  $V_s$  and  $V_{ns}$  profiles for  $T = 1.65$  K and the channel width  $H = 0.1$  cm. Solid lines correspond to the parabolic  $V_n$  with  $U_c = 1.5$  cm/s, dot-dashed line to  $U_c = 2$  cm/s, and dashed line to the flattened profile of  $V_n$ .

compare the changes in the shape of the tangle, plotting in Figs. 10 and 11 the dimensionless VLD  $\mathcal{L}^\dagger(x)$  for the core and for the near-wall regions, rescaled to the tangle width at each of the presented three time moments. In this way, the scaled coordinate  $X = 0$  corresponds to the cold edge of the tangle and  $X = 1$  corresponds to the hot edge. The earliest time moment corresponds to the time when the three-dimension (3D) tangle was formed and the latest to the time when the bulk region and two fronts are fully developed.

The tangle dynamics for the parabolic  $V_n$  profile is shown in Fig. 10. The main feature of these profiles is the asymmetry with respect to the center of the tangle. The near-wall profiles, shown by dashed lines, rise along all tangle length and the asymmetry is relatively mild. The core profiles, shown by solid lines, on the other hand, are very asymmetric, with the hot side growing faster than the cold side. We can see that at  $T = 1.3$  K [Fig. 10(a)] the growth of the cold side in the core is stalled compared to the near-walls profiles. This results in the wall-normal profiles with a significant difference between VLD at the core and near the walls [cf. Fig. 5(a)]. Moreover,

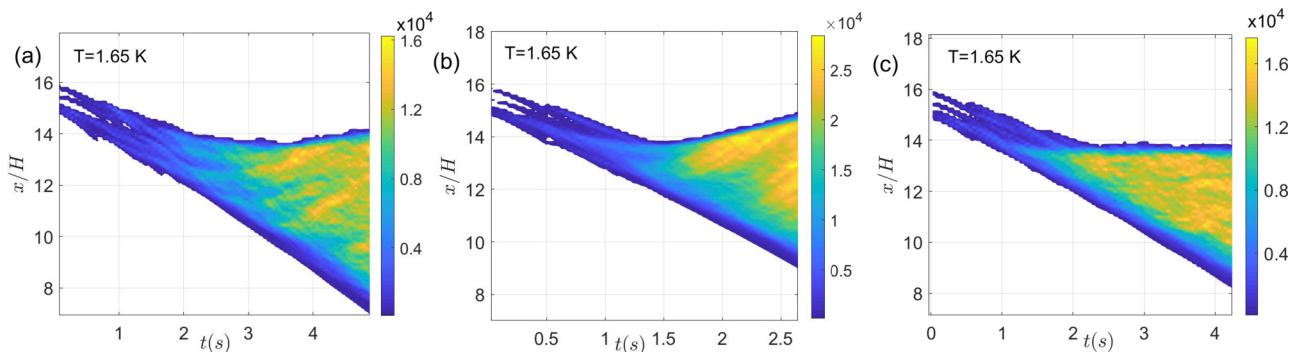


FIG. 9. VLD dynamics for  $T = 1.65$  K and various  $V_n$  profiles: (a) parabolic profile with  $U_c = 1.5$  cm/s, (b) parabolic profile with  $U_c = 2$  cm/s, and (c) flattened  $V_n$  profile, corresponding to (a).

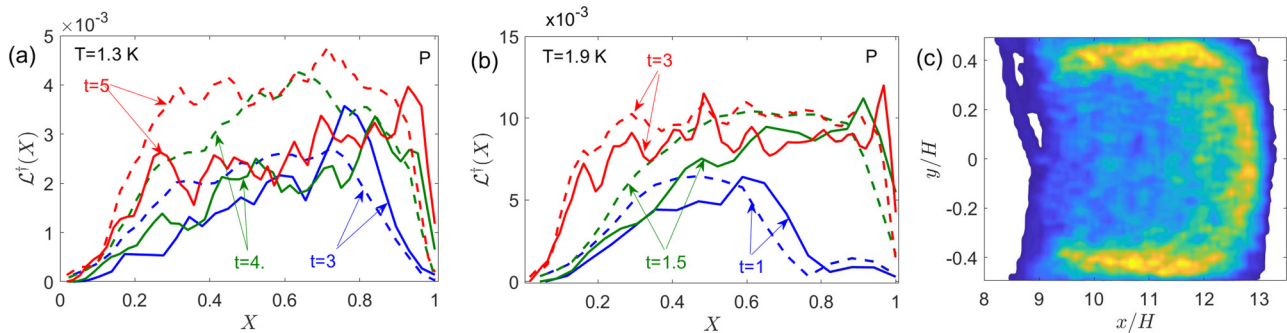


FIG. 10. Rescaled dimensionless VLD profiles  $\mathcal{L}^\dagger(x)$  for the parabolic  $V_n$  at various time moments for (a)  $T = 1.3$  K,  $U_c = 3$  cm/s, and (b)  $T = 1.9$  K,  $U_c = 1$  cm/s in the narrow channel  $H = 0.1$  cm. Solid lines denote the core VLD profile, dashed lines denote the near-wall profiles. (c) 2D VLD map  $\mathcal{L}(x, y)$  for  $T = 1.3$  K,  $U_c = 3$  cm/s, and  $H = 0.15$  cm.

during all evolution, the core region leads in the hot front, while the wall region develops faster at the cold front.

Similar tendencies in the dynamics are observed at  $T = 1.9$  K, Fig. 10(b). The main difference from the lower temperature regime is faster tangle development and closer values of  $\mathcal{L}^\dagger$  in the wall and the core region, in accordance with Fig. 5(c). Notably, also here the core region first develops closer to the hot front (i.e. in the direction of  $V_n$ ), even though  $V_s$  in the core is oriented in this case in the opposite direction.

The main reason for this asymmetry is the spatial distribution of the driving velocity. As is shown in Appendix D, due to enhanced VLD production in the channel core in the hot front region, and the transverse VLD flux that moves the vortex lines toward the walls, the parabolic wall-normal profile of the normal-fluid is translated into a transient VLD distribution that reminds a horseshoe shape:  $\mathcal{L}$  is higher near the walls and near the hot edge in the core of the channel, as is shown in Fig. 10(c). The clearly visible hump in the earliest core VLD profile [e.g., blue solid line, labeled  $t = 3$  in Fig. 10(a)] corresponds to the central part of the horseshoe. With the development of the tangle, the hump is redistributed to the rest of the core region and becomes less prominent, although it does not disappear completely even when the bulk value of  $\mathcal{L}$  is established over a large part of the core. This horseshoe shape of the densest part of the growing tangle lasts longer for larger  $U_c$  and wider channels. Such an asymmetry of the tangle, that appears from the very beginning of the

tangle development leads to very different initial conditions for the formation of plug fronts (see also Appendix D).

One may argue that such a scenario may not be realized in the real counterflow due to flattening of the normal-fluid profile and therefore more even initial VLD distribution. However, as we show in Figs. 11, 26(c) and 26(f), the streamwise tangle asymmetry is initially present even if the flattened  $V_n(y)$  is imposed, with VLD growing faster at the hot edge of the plug. This transient behavior does not last long in this case, however, the hot front remains steeper than the cold front, similar to the tangles formed under the parabolic  $V_n$ .

### F. Large-scale superfluid motion

In simulations of homogeneous tangles under triply periodic boundary conditions, the presence of mean normal-fluid and superfluid velocities is accounted for by a constant and space-homogeneous counterflow velocity, while the tangle-induced velocity is artificially randomized by interactions with image vortex lines. In simulations of superfluid turbulence in the channel with periodic streamwise conditions, the translation invariance is broken in the wall-normal direction, creating superfluid motion from the center of the channel towards the walls. Still, in the streamwise direction, the variation of the vortex lines velocity is not taken into account.

In our simulations, the tangle has finite streamwise length and the superfluid velocity varies along the tangle as well as

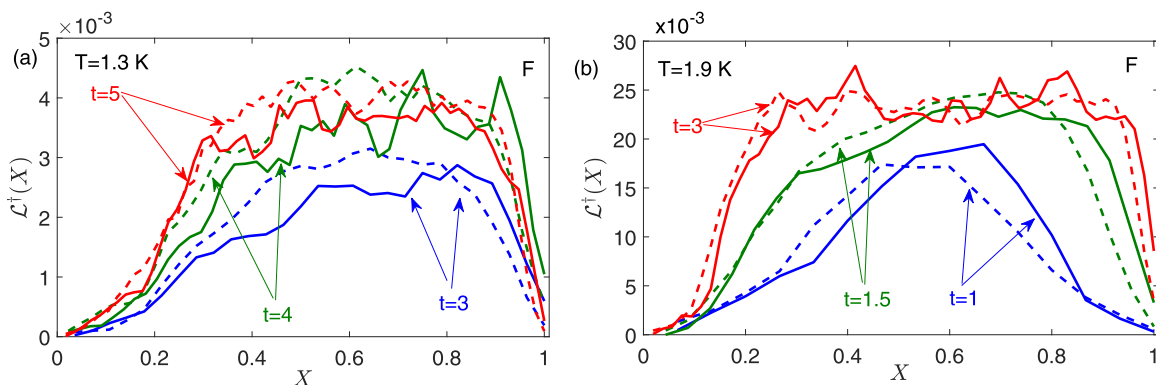


FIG. 11. Rescaled dimensionless VLD profiles  $\mathcal{L}^\dagger(x)$  for the flattened  $V_n$  at various time moments for (a)  $T = 1.3$  K,  $U_c = 3$  cm/s and (b)  $T = 1.9$  K,  $U_c = 1$  cm/s. Solid lines denote the core VLD profile, dashed lines denote the wall profiles.



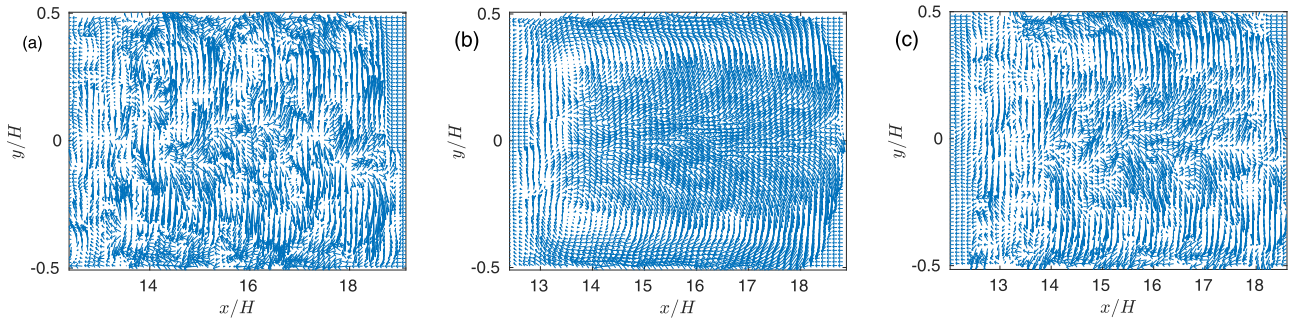


FIG. 12. Tangle drift velocity  $\mathbf{V}_{\text{drift}}$  for  $T = 1.3$  K and (a)  $U_c = 2$  cm/s, (b)  $U_c = 4$  cm/s, and (c) flattened  $V_n$  profile. The arrows direction shows the local orientation of the velocity, the size of the arrows is proportional to its magnitude.

across it. The drift velocity of vortex lines  $\mathbf{V}_{\text{drift}}$  that includes the mean velocity as well as all contributions of the tangle-induced velocity represent the superfluid motion at all scales that are formed in our system. In Fig. 12, we plot the tangle drift velocity for  $T = 1.3$  K, at which the mean superfluid velocity does not dominate and motion at all scales are clearly seen. Since near the wall the superfluid flows toward smaller  $x$ , while in the core its motion is oriented toward larger  $x$  values, eddies of various sizes are formed. For parabolic  $V_n$  profile, at weak driving velocity  $U_c = 2$  cm/s, Fig. 12(a), many circular eddies with sizes that are much larger than the intervortex distance  $\ell$  but smaller than the channel size  $H$ , are formed. At the strong driving velocity  $U_c = 4$  cm/s, Fig. 12(b), two dominant vortices of the system size  $H/2$  and opposite circulation orientation, covering whole tangle length are formed, with smaller motions masked by the largest ones. When the flow is driven by flattened  $V_n$  profile, Fig. 12(c), we can see both the system size motion and smaller eddies. Please note that near the walls the tangle velocity contributions are oriented perpendicular to the channel walls due to no-slip boundary conditions. It is the mean superfluid velocity that moves the vortex lines near the walls and helps to create the large-scale eddies. At higher temperatures, the dominant  $\mathbf{V}_s^0$  sweeps the tangle along the channel and masks the presence of smaller superfluid motions, similar to the sweeping velocity in classical fluids. However, analysis of the relative drift velocity  $\mathbf{V}_{\text{drift}} - \mathbf{V}_s^0$  shows the presence of these motions also in the vortex tangles at higher  $T$ .

### G. Structural parameters $c_2^2$ and $I_\ell^\dagger$

In the microscopic description [16] of the tangle dynamics very important role is played by two structural parameters: the local binormal  $\mathbf{I}_\ell = \langle \mathbf{s}' \times \mathbf{s}'' \rangle$  and the ratio  $c_2^2$  between the mean-square curvature and the vortex line density. These parameters contribute to the terms of the equation of motion for  $\mathcal{L}$ , responsible for the production and annihilation of the vortex line length, respectively [cf. Eqs. (11)–(15)]. In the homogeneous tangles, these parameters are constants, while in the channel flow they depend on the position in the channel. The behavior of these parameters at the edges of the tangle was not studied so far.

The profiles of the coefficient  $c_2^2$  are shown in Fig. 13 for  $T = 1.3$  K [panels (a)–(c)] and for  $T = 1.9$  K [panels (e)–(f)]. There are several common properties of the streamwise profiles [panels (a), (b), (d), and (e)], independent of the

temperature and the type of the driving velocity. The values of  $c_2^2$  exhibit fluctuations along the tangle with a relatively large amplitude, especially when the flow is driven by the parabolic  $V_n$ . The fluctuations are less pronounced in the wall-normal profiles [panels (c) and (f)]. These profiles have a somewhat different averaging scope, however, we are inclined to attribute these fluctuations to the streamwise inhomogeneity of both VLD and the curvature, that do not match exactly. Nevertheless, the values of  $c_2^2$  are fairly constant along the tangle, with the same values observed also the hot front region. The behavior of  $c_2^2$  in the cold front regions is different, with the tendency of becoming larger at low  $T$ . Similar behavior is observed for other values of  $U_c$  (not shown).

When the flow is driven by the flattened  $V_n$  profile, the values of  $c_2^2$  may be considered almost constant across the channel. Its behavior changes only within the intervortex distance from the wall, where the values of VLD drop very quickly, while the square curvature keeps its values almost until the wall. Conversely, when the driving velocity has the parabolic profile,  $c_2^2$  has the largest values in the center of the channel and decreases linearly towards the walls until the intervortex distance is reached. Then it increases, in a similar way as for the flattened  $V_n$  profile, even reaching similar values at the wall. These larger values in the core of the channel, as compared to the near-wall region, are observed along the entire tangle bulk and in the hot front. On the other hand, the values of  $c_2^2$  in the flows driven by flattened  $V_n$  may be considered almost space-homogeneous, except for the cold front and very near the walls, and similar to the values of  $c_2^2$  in the channel core, observed for the parabolic normal flow.

The dominant contribution to the production of vortex lines has the term [16] that depend on the streamwise projection of the local binormal  $I_{\ell,x}$ . In Fig. 14, we plot its values normalized by the mean curvature  $I_{\ell,x}^\dagger = I_{\ell,x}/\varkappa$ . The general behavior of  $I_{\ell,x}^\dagger$  is similar to that of  $c_2^2$ . We, therefore, point out the main differences. Looking at the wall-normal profiles, Figs. 14(c) and 14(f), we notice that  $I_{\ell,x}^\dagger$  is almost homogeneous over the channel core for parabolic flows at both temperatures, crossing over to a linear decrease toward the walls beyond the core region. It does not increase significantly very near the wall, although at  $T = 1.3$  K a kink is observed. This kink becomes stronger for wider channels and appears at  $T = 1.9$  K for wide channels as well. For the flow, driven by the flattened normal-fluid velocity profile, the core values

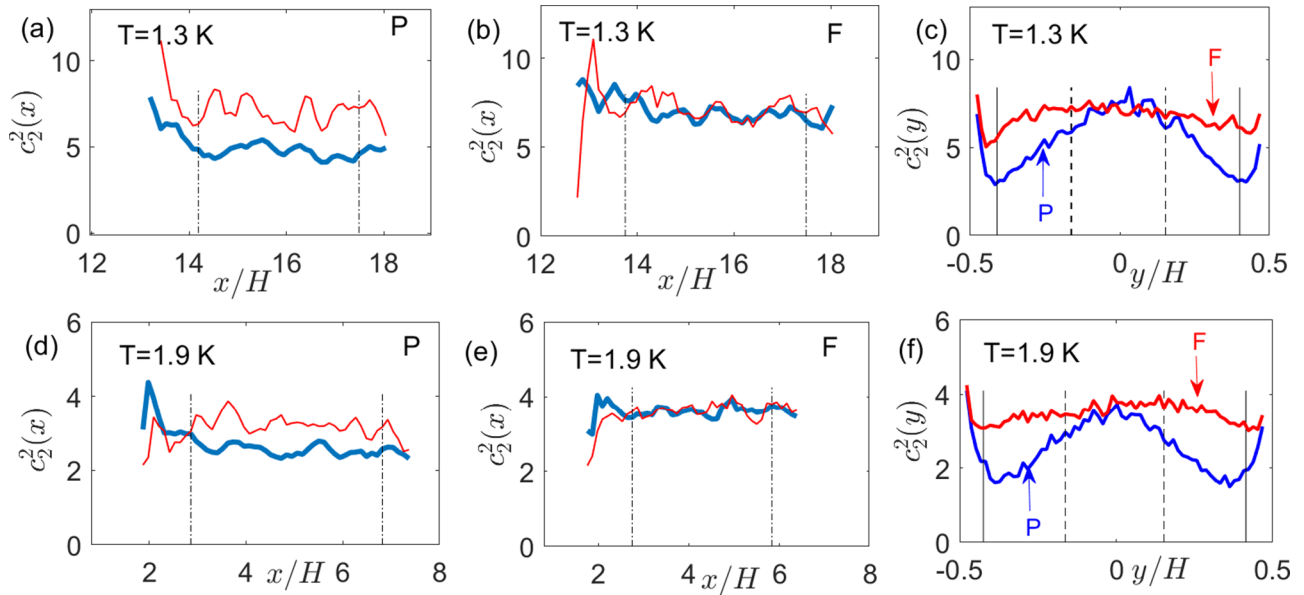


FIG. 13. The coefficient  $c_2^2$  at various conditions. The profiles for  $T = 1.3$  K are shown in the top row: the streamwise profiles for (a) the parabolic  $V_n$  with  $U_c = 3$  cm/s, labeled P, (b) the flattened profile, labeled F, (c) the corresponding wall-normal profiles. The profiles for  $T = 1.9$  K are shown in the bottom row: (d) the parabolic  $V_n$  with  $U_c = 1$  cm/s and (e) the flattened profile; (f) the corresponding wall-normal profiles. The dot-dashed and dashed black lines mark the edges of the bulk and the core regions for the streamwise and for the wall-normal profiles, respectively. Thin solid lines in (c) and (f) are placed at the intervortex distance from the corresponding walls.

of  $I_{\ell,x}^\dagger$  extend further toward to walls, especially at high  $T$ . Nevertheless, the difference between the mean values of the channel core and the near-wall region persists along the tangle bulk, even in this case. The values of  $I_{\ell,x}^\dagger$  in both fronts regions differ from the bulk, even if we take into account strong fluctuations in its streamwise distribution.

Interestingly, the shape of wall-normal profiles of  $c_2^2$  and  $I_{\ell,x}$  in the flows, generated by the flattened  $V_n$  profiles, does not depend on  $V_{ns}$  and the channel width at both high and low  $T$ , although for different reasons. At low  $T$ , the curvature is only weakly dependent on the distance from the wall, while VLD strongly peaks near the walls. At high  $T$ , wall-normal

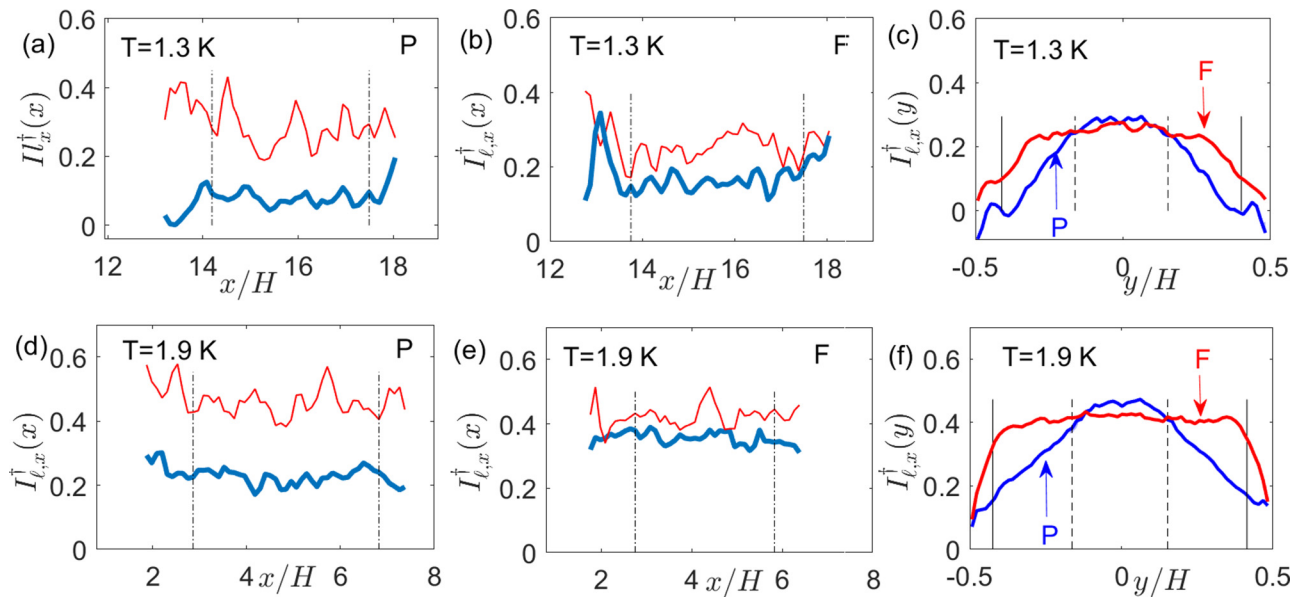


FIG. 14. The streamwise component of the index  $I_{\ell,x}^\dagger$  at various conditions. The profiles for  $T = 1.3$  K are shown in the top row: the streamwise profiles for (a) the parabolic  $V_n$  with  $U_c = 3$  cm/s, labeled P, (b) the flattened profile, labeled F, (c) the corresponding wall-normal profiles. The profiles for  $T = 1.9$  K are shown in the bottom row: (d) the parabolic  $V_n$  with  $U_c = 1$  cm/s and (e) the flattened profile; (f) the corresponding wall-normal profiles. Vertical dot-dashed lines mark the edges of the bulk of the streamwise profiles, vertical dashed lines mark the edges of the core for the wall-normal profiles. Thin solid lines in (c) and (f) are placed at the intervortex distance from the corresponding walls.

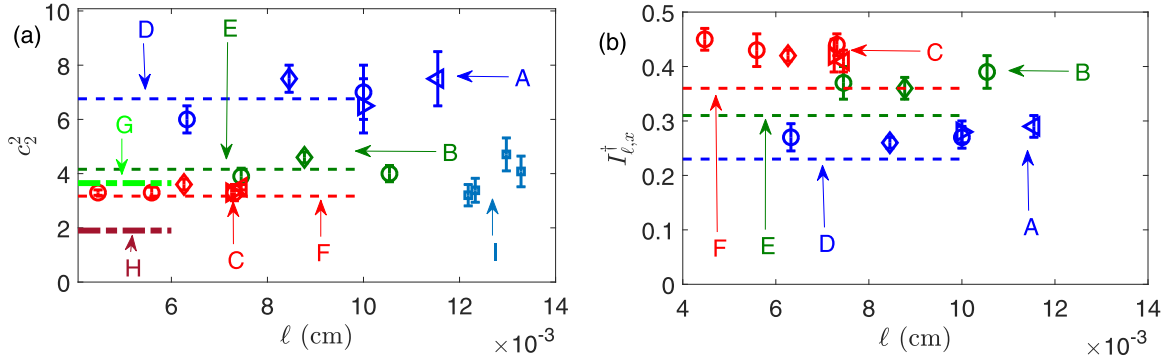


FIG. 15. The mean values of (a)  $c_2^2$  and (b)  $I_{l,x}^\dagger$  in the core of the channel. The labels (A–C) correspond to current simulations (A:  $T = 1.3$  K, blue symbols, B:  $T = 1.65$  K, green symbols, C:  $T = 1.9$  K, red symbols). Different flow conditions are represented by different symbols:  $\circ$  denote front velocities for the parabolic  $V_n$  and various  $U_c$ ,  $\diamond$  corresponds to the flattened  $V_n$  profile,  $\triangleright$  and  $\triangleleft$  denote channel width  $H = 0.15$  and  $0.2$  cm, respectively. The error bars denote standard deviation from the mean in the bulk of the tangle. Dashed horizontal lines, labeled D–F ( $T = 1.3$ ,  $1.6$ , and  $1.9$  K, respectively) are the values of  $c_2^2$  and  $I_l^\dagger$  for the homogeneous tangle from Ref. [39] with the GEC reconnection criterion, the same as used in this paper. In (a), thick dot-dashed lines, labeled G ( $T = 1.65$  K) and H ( $T = 1.95$  K), denote the experimental values of  $c_2^2$  from Ref. [44] in the range of intervortex distances  $4 \times 10^{-3}$ – $6 \times 10^{-3}$  cm. Filled squares with error-bars, labeled I, denote the results of simulations in the channel with parallel solid plates from Ref. [28] in the range of temperatures  $T = 1.4$ – $1.7$  K.

profiles of  $\mathcal{L}$  are more homogeneous, but the curvature, in this case, decreases toward the walls more strongly. The resulting  $y$  distributions of  $c_2^2$ , Figs. 13(c) and 13(f), are very similar. The wall-normal distribution of  $I_{l,x}^\dagger$  is fully defined by the streamwise component of the binormal that is large in the center of the channel and quickly decreases toward the walls. Its shape is only slightly altered by similar distribution of  $\langle |s''| \rangle$ , Figs. 14(c) and 14(f).

To get an idea of how these results are related to other known measurements, we compare in Fig. 15(a) the values of  $c_2^2$  for the channel core with the results of simulations of the homogeneous tangles [39], in the planar channel [28] and with the experimental results [44] for the range of intervortex distances, typical for our simulations. We have chosen to compare the values for the core of the channel because the experiments were carried out in wide channels, where the core behavior is expected to dominate. These values are also expected to be more comparable with  $c_2^2$  in the homogeneous tangle.

As is clearly seen, the calculated values of  $c_2^2$  do not depend on the intervortex distance within the range used in our simulations. The temperature dependence agrees with previous results, i.e., larger  $c_2^2$  at lower temperatures. Our current results agree well with the values obtained in the homogeneous vortex tangles [39], shown by thin dashed lines. The values of  $c_2^2$  obtained in numerical simulations of the vortex tangle in the flow between parallel plates [28] for temperatures between  $1.4$ – $1.7$  K are shown by filled squares. The values of  $c_2$  were calculated as averages over the whole channel and are expected to be lower than the values in the channel core. With this in mind, they agree reasonably well with our results for  $T = 1.65$  K.

The experimental values calculated using the fit [44] for  $T = 1.65$  K, shown by thick dot-dashed lines, are somewhat smaller, but not far from the numerical results. Here we need to take into account that in the considered range  $\ell = 4 \times 10^{-3}$ – $6 \times 10^{-3}$  cm, the fit becomes unreliable and the experimental points tend to scatter, see Fig. 11 in Ref. [44].

The experimental values for  $T = 1.95$  K are expectedly lower than our results for  $T = 1.9$  K.

Similar measurements of  $I_{l,x}^\dagger$  in the channel core are shown Fig. 15(b). Note that this parameter measures alignment of the local velocity  $\mathbf{V}_{loc}$  with the direction of the counterflow velocity. Similar to  $c_2^2$ , the index  $I_{l,x}^\dagger$  is fairly constant for a given temperature, being larger for higher  $T$ . These values are somewhat higher than those obtained in the homogeneous tangles [39], including the values obtained in the flow driven by the flattened normal-fluid profile (marked by diamond symbols). The temperature mismatch ( $T = 1.65$  K in our simulation versus  $T = 1.6$  K in Ref. [39]) may account for the difference at the intermediate temperature, however, the trend is systematic across the temperatures.

### III. FRONT DYNAMICS AND ANALYSIS OF THE VLD BALANCE EQUATION

#### A. Background overview

Interface motion and front propagation in fluids are subject of intensive studies in various fields of knowledge. Perhaps most well known are chemical reaction fronts in liquids [45], population dynamics of ecological communities [46], and combustion [47]. The mathematical description of those phenomena is based on partial differential equations (PDE) for the evolution of the concentration of the reacting species and the evolution of the velocity field. The two PDEs for the reactants and the velocity field are usually coupled, often in a nontrivial way. A mathematical simplification can be obtained by neglecting the back-reaction of the reactant on the velocity field, which evolves independently. Such simplification is usually justified for the laminar velocity field. Even in such a limit, the front dynamics is still nontrivial and it is described by a so-called *advection-reaction-diffusion* (ARD) equation

$$\partial\theta/\partial t + \mathbf{u}(\mathbf{r}, t) \cdot \nabla\theta = D\nabla^2\theta + F(\theta), \quad (5)$$

where  $\theta(\mathbf{r}, t) \in [0, 1]$  is the reactant concentration,  $\mathbf{u}$  is the advection velocity field,  $D$  is the diffusivity and  $F(\theta)$  is

the reaction term. The front interface is in general two-dimensional, although in many cases it is sufficient to consider its motion only in one direction. In a typical model situation, the localized initial conditions are used, i.e.,  $\theta(\mathbf{r}, 0) \rightarrow 1$  exponentially fast when  $\mathbf{r} \rightarrow -\infty$  and  $\theta \rightarrow 0$  exponentially fast when  $\mathbf{r} \rightarrow \infty$ . In this case, the reaction front will move towards positive  $r$ . Here,  $\theta = 0$  is an unstable state and  $\theta = 1$  is a stable one, therefore  $F(\theta)$  satisfies the condition

$$F(0) = F(1) = 0, \quad F(\theta) > 0, \text{ if } 0 < \theta < 1. \quad (6)$$

It was shown [48,49] that if there is no advection, the front speed converges to a limiting velocity  $v_0$ , defined by a marginal stability condition. In a moving fluid, it is natural to expect [50,51] that the front will propagate with an average (turbulent) speed  $v_f > v_0$ . The turbulent front speed  $v_f$  is defined by relative importance of the flow characteristics, such as the relevant system size  $\Lambda$ , advection velocity  $u$ , the diffusivity  $D$ , and the typical time scale  $\tau_r$  of the reaction term  $F(\theta) = f(\theta)/\tau_r$ . The shape of  $F(\theta)$ , or more specifically the value  $\theta$  at which it has largest slope, also plays a very important role. Two types of its functional dependence are of particular importance: (i) a Fischer-Kolmogorov-Petrovskii-Peskunov (FKPP) nonlinearity [45,46]  $F(\theta) = \theta(1 - \theta)$ , or in general, any convex function  $F''(\theta) < 0$ ; (ii) an Arrhenius (or ignition) nonlinearity [51]  $F(\theta) = \exp^{-\theta_c/\theta}(1 - \theta)$ . Here the parameter  $\theta_c$  is an activation concentration, below which there is almost no production.

In case of FKPP nonlinearity, the maximum slope  $F(\theta)$  occurs at  $\theta = 0$ . Such fronts are called *pulled* fronts and their dynamics is fully determined by the region  $\theta \approx 0$ , as if pulled by the leading edge. When the maximum slope of  $F(\theta)$  occurs at  $\theta > 0$ , the front is *pushed* by the nonlinear interior. The allowed velocity of the pulled fronts has to satisfy the condition [45,50]

$$2\sqrt{DF'(0)} \leq v_{\min} < 2\sqrt{D \sup_{\theta} \frac{F(\theta)}{\theta}}, \quad (7)$$

where  $F(\theta)/\theta$  is the measure of the growth rate. For FKPP dynamics,  $F(\theta)/\theta = F'(0)$  and for the localized initial conditions Eq. (7) become an equality  $v_{\min} = v_0 = 2\sqrt{DF'(0)}$ .

For pushed fronts, the minimal front velocity  $v_{\min}$  is always larger than  $v_0$ . In both cases, depending on the steepness of the initial conditions the asymptotic front speed may relax to the minimal  $v_{\min}$  or remain larger.

There exists a vast literature on the front propagation in various flows. We concentrate on the laminar shear flow of ADR type and summarize several important results (for details see Refs. [50,51] and references therein):

(1) The front velocity is bounded by  $K_1 u < v_f < v_0 + K_2 u$ , where the limiting velocity  $v_0 = 2\sqrt{D_0 \sup_{\theta} [F(\theta)/\theta]}$  and the diffusivity  $D_0$  are the parameters in the absence of the advection flow,  $K_1$  and  $K_2$  are flow-dependent parameters.

(2) The diffusive transport is enhanced by the incompressible flow, resulting in an effective diffusion coefficient  $D_{\text{eff}} > D_0$ .

(3) In the presence of advection, the bound on limiting velocity may be modified as  $v_f \leq 2\sqrt{D_{\text{eff}} \sup_{\theta} [F(\theta)/\theta]}$ .

## B. ARD-type equation for VLD

Now we return to the channel counterflow of the superfluid  $^4\text{He}$  and relate the properties of the model system, described in the previous section, to the dynamics of the turbulent vortex tangle.

Here the role of the dimensionless variable  $\theta$  in advection-reaction-diffusion equation (5) is played by the normalized VLD  $L = \mathcal{L}/\mathcal{L}_0$ , where  $\mathcal{L}_0$  is the equilibrium vortex line density in the bulk of the tangle. The equation of motion for  $L(\mathbf{r}, t)$  in the channel may be written as

$$\partial_t L(\mathbf{r}, t) + \nabla \mathcal{J}(\mathbf{r}, t) = \tilde{D} \nabla^2 L(\mathbf{r}, t) + F[L(\mathbf{r}, t)], \quad (8)$$

$$\mathcal{J}(\mathbf{r}, t) = \mathbf{V}_{\text{drift}}(\mathbf{r})L(\mathbf{r}, t), \quad (9)$$

where  $\tilde{D}$  is the effective diffusivity of VLD and  $\mathcal{J}(\mathbf{r}, t)$  is the VLD flux. We follow Schwarz's microscopic approach [16] and recall that the rate of elongation of the vortex line segment  $\delta\xi$  is

$$\begin{aligned} \frac{1}{\delta\xi} \frac{d\delta\xi}{dt} &= \alpha(\mathbf{V}_{\text{ns}}(\mathbf{s}, t) \cdot (\mathbf{s}' \times \mathbf{s}'') - |\mathbf{s}' \times \mathbf{s}''|^2) \\ &\quad + \mathbf{s}' \cdot \mathbf{V}_{\text{nl}}' - \alpha \mathbf{s}'' \cdot \mathbf{V}_{\text{ns}}. \end{aligned} \quad (10)$$

Integration of Eq. (10) over the vortex tangle gives for the RHS term  $F(L)$ :

$$F = \mathcal{P}_1 + \mathcal{P}_2 + \mathcal{P}_3 - \mathcal{D}, \quad (11)$$

$$\mathcal{P}_1 = \frac{\alpha}{\mathcal{L}_0 V'} \int_{\Omega'} (\mathbf{V}_{\text{ns}}^0 - \mathbf{V}_{\text{nl}}) \cdot (\mathbf{s}' \times \mathbf{s}'') d\xi, \quad (12)$$

$$\mathcal{P}_2 = \frac{1}{\mathcal{L}_0 V'} \int_{\Omega'} \mathbf{s}' \cdot \mathbf{V}_{\text{nl}}' d\xi, \quad (13)$$

$$\mathcal{P}_3 = -\frac{\alpha'}{\mathcal{L}_0 V'} \int_{\Omega'} \mathbf{s}'' \cdot \mathbf{V}_{\text{ns}} d\xi, \quad (14)$$

$$\mathcal{D} = \frac{\alpha}{\mathcal{L}_0 V'} \int_{\Omega'} \mathbf{V}_{\text{loc}} \cdot (\mathbf{s}' \times \mathbf{s}'') d\xi. \quad (15)$$

Here,  $\mathcal{P}_1$  is usually named the production term since it is responsible for most of the vortex line elongation. The last term  $\mathcal{D}$  is traditionally termed the decay term since it represents the annihilation of vortex-line length during vortex dynamics and reconnections. Two other terms  $\mathcal{P}_2$  and  $\mathcal{P}_3$  also represent the production of the vortex-line length. In the homogeneous tangle,  $\mathcal{P}_3$  vanish by symmetry. The term  $\mathcal{P}_2$  is usually omitted due to smallness. We include all terms since  $\mathcal{P}_2$  and  $\mathcal{P}_3$  become non-negligible at low  $T$  near the walls (see Appendix D). Each term is proportional to  $L$  due to integration over  $d\xi$  and division by  $\mathcal{L}_0$ . At this stage, we retain the integral representation of  $F(L)$ .

Using the same approach, the VLD flux Eq. (9) is defined as

$$\mathcal{J} = \frac{1}{\mathcal{L}_0 V'} \int_{\Omega'} \mathbf{V}_{\text{drift}} d\xi = \mathbf{V}_{\text{s}}^0 L + \frac{1}{\mathcal{L}_0 V'} \int_{\Omega'} (\mathbf{V}_{\text{bs}} + \mathbf{V}_{\text{mf}}) d\xi. \quad (16)$$

As was shown in Sec. II D, the bulk VLD and other tangle properties in the core of the channel and near the walls are different but well defined. Therefore, instead of taking into account the full 3D structure of the tangle, as well as the 2D front interface, we consider the dynamics of the core

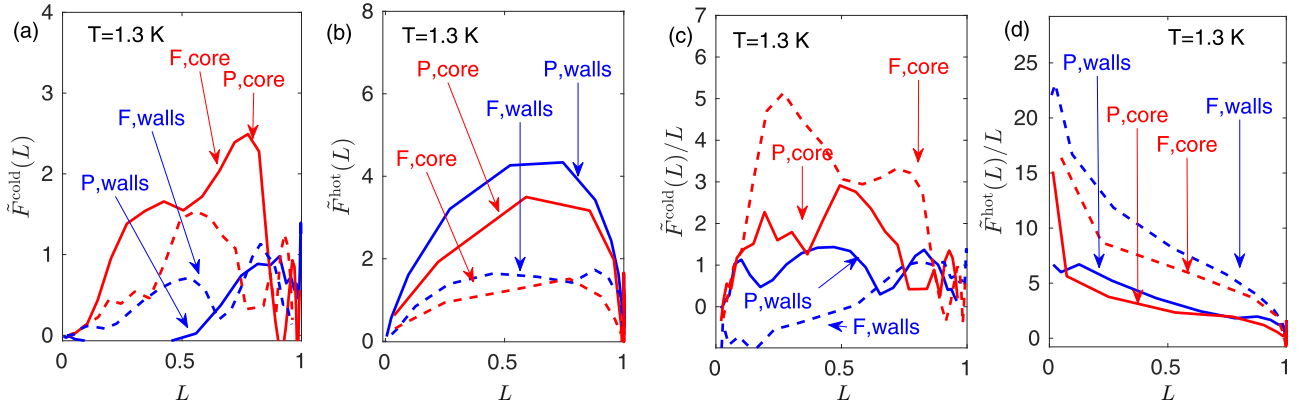


FIG. 16. The profiles of  $\tilde{F}^j(L)$  vs  $L$  [(a) and (b) for the cold and hot fronts, respectively] and  $\tilde{F}^j(L)/L$  vs  $L$  [(c) and (d) for the cold and hot fronts, respectively] for  $T = 1.3$  K. The profiles for the parabolic  $V_n$  are shown by solid lines, the profiles for the flattened  $V_n$  are shown by dashed lines and denoted as P and F, respectively. The lines for the channel core and the near-wall region are labeled in the figure.

and the wall regions separately as one-dimensional (1D). However, to get the 1D equation for  $L(x)$ , it is not sufficient to only account for the streamwise component of Eq. (8). Although the transverse diffusion is negligible, the transverse VLD flux  $\mathcal{J}_y$  is an important factor in the inhomogeneous tangle dynamics [29–31], moving VLD from the channel core towards the walls. We move it to RHS of Eq. (8), such that after averaging of the core and walls regions, it will serve as an additional decay term in the channel core and as an additional production term near the walls. In such a way, we get the ARD-type equation for the normalized VLD  $L(x, t)$  for the core ( $j = \text{core}$ ) and for the walls ( $j = \text{wall}$ ) regions:

$$\frac{\partial L^j(x, t)}{\partial t} + \frac{\partial \mathcal{J}^j(x, t)}{\partial x} = \tilde{D}^j \frac{\partial^2 L^j(x, t)}{\partial x^2} + \tilde{F}^j[L(x, t)], \quad (17)$$

$$\begin{aligned} \mathcal{J}^j(x, t) &= V_s^0 L^j(x, t) + \tilde{\mathcal{J}}_x^j(x, t) \\ \tilde{F}^j[L(x, t)] &= F^j[L(x, t)] - \frac{\partial \mathcal{J}_y^j(x, t)}{\partial y}. \end{aligned} \quad (18)$$

The longitudinal tangle-induced flux  $\tilde{\mathcal{J}}_x = \mathcal{J}_x - V_s^0 L$  helps to redistribute the vortex line density along the tangle. We account for it by replacing  $V_s^0 \rightarrow V_s^x$ . Here we neglected the streamwise component of the mutual friction contribution to the drift velocity  $V_{\text{mf}}^x$  since it contributes only about 1% to the value of  $V_{\text{drift}}^x$ . The modified production term  $\tilde{F}^j[L(x, t)]$  includes the contribution from the transverse flux. Since, in this formulation, the effective diffusivity is a parameter that depends on the flow conditions, we allow for different values of  $\tilde{D}^j$  for the channel core and for near-wall regions. Moreover, the values may differ in the tangle bulk and in the fronts regions.

Using this framework, we analyze in the rest of this section various aspects of the propagation of the fronts, including the type of the fronts, their speeds, shapes, and the effective diffusivity.

### C. Properties of $\tilde{F}(L)$

To identify the type of nonlinearity in the Eq. (17), we calculate the front profile for  $\tilde{F}(L)$ , as described in Appendix C.

The dependencies of  $\tilde{F}(L)$  and  $\tilde{F}(L)/L$  on  $L$  in the front regions, calculated for  $T = 1.3$  K, are shown in Fig. 16. The results for the parabolic profile as shown by solid lines, for the flattened profile by dashed lines. As is clearly seen, the  $L$  dependence of  $\tilde{F}(L)$  is different for the cold fronts [panel (a)] and for the hot fronts [panel (b)]. The hot fronts are of the FKPP type, i.e. the largest rate of growth  $\sup_L[\tilde{F}(L)/L]$  is at  $L \rightarrow 0$ , as is shown in Fig. 16(d), while for the cold fronts [Fig. 16(c)], it is found closer to the center part of the front. This property is robust and observed all flow conditions, and for both types of the  $V_n$  profiles, although at  $T = 1.9$  K the maximum growth rate for the cold front is found closer to  $L = 0$  than at low  $T$ .

Despite complicated shapes of  $\tilde{F}(L)$  for various flow conditions, the values of the largest rate of growth  $\sup_L[\tilde{F}(L)/L]$ , shown in Fig. 17, depend linearly on  $V_s^0$ . The dependencies for the near-wall and the core regions differ even for the same front region, with hot fronts being stronger dependent on the advection velocity than the cold fronts. In particular,  $\sup_L[\tilde{F}(L)/L]$  for the cold front in the channel core is almost  $V_s^0$  independent.

Most of the attempts to find the equation of motion for the vortex line density so far dealt with steady-state tangles and represented  $\mathcal{P}_1$  and  $\mathcal{D}$  in Eq. (11) as functions of  $\mathcal{L}$  and  $V_{\text{ns}}$  only for the homogeneous tangles, adding the curvature, the binormal, and their derivatives [17–19] in the inhomogeneous case. In the current situation of the inhomogeneous and growing tangle, we can not expect a unique closure. Aiming at the analysis of front dynamics, we make use of the fact that at least the hot fronts are of FKPP type. We then seek to represent Eq. (18) in a general form

$$\tilde{F}(L) = \mathcal{A}L - \mathcal{B}L^2, \quad (19)$$

where the coefficients  $\mathcal{A}$  and  $\mathcal{B}$  have dimensions [1/s] and may depend on the position and time.

### D. Closure for $\tilde{F}(L)$

The main idea behind all the proposed closures [16,29] is to take slowly varying fields out of the average along the vortex lines. The resulting closure form is a product of slowly varying macroscopic properties of the flow [such as  $\mathbf{V}_{\text{ns}}(x, y, t)$ ] and of

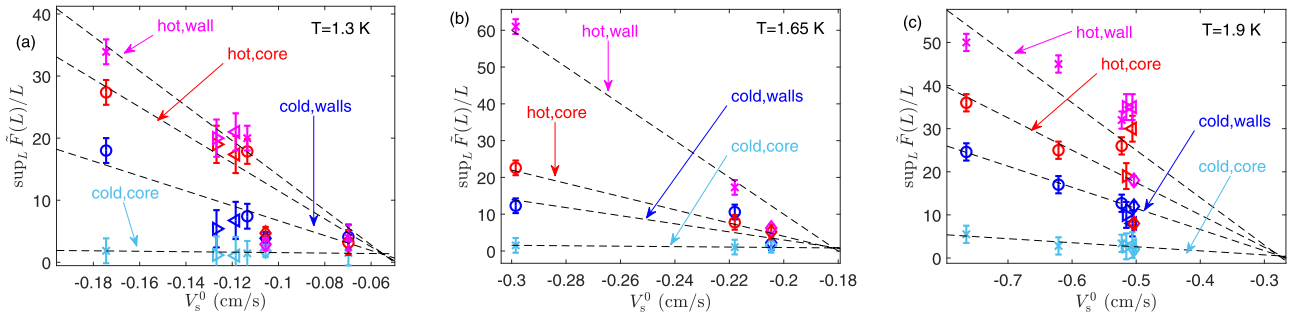


FIG. 17. Maximum growth rate  $\sup_L[\tilde{F}^j(L)/L]$  at various flow conditions. In all panels,  $\circ$  denote front velocities for parabolic  $V_n$  and various  $U_c$ ,  $\diamond$  corresponds to the flattened  $V_n$  profile,  $\triangleright$  and  $\triangleleft$  denote channel widths  $H = 0.15$  and  $0.2$  cm, respectively. The linear dependence on  $V_s^0$  is shown by dashed lines, which serve to guide the eye only. Different data sets are marked in the figure by labels of the same color that point to the corresponding symbols.

the tangle [such as  $c_2^2(x, y, t)$  and  $I_{\ell,x}(x, y, t)$ ]. In Appendix D, we discuss various contributions to the  $\tilde{F}(L)$ . For our current analysis, however, we do not need all of them.

We start with the last term in Eq. (19). It is readily associated with the term  $\mathcal{D}$ , Eq. (15), as the relation  $\mathcal{D} \propto \mathcal{L}^2$  was shown experimentally [52,53] and rationalized theoretically [3,16] for the steady-state homogeneous vortex tangles. We use here the following form [29] of this dependence for the dimensionless VLD  $L$ :

$$\mathcal{D} \approx \alpha\beta\langle\kappa^2\rangle L = \mathcal{B}L^2; \quad \mathcal{B} = \alpha\beta c_2^2 \mathcal{L}_0, \quad (20)$$

where the relation  $\langle\kappa^2\rangle = c_2^2 \mathcal{L}$  was used. In the homogeneous tangle, where  $c_2^2$  is a constant, the coefficient  $\mathcal{B}$  is also a constant for a given temperature. In the inhomogeneous developing tangle, the mean-square curvature  $\langle\kappa^2\rangle$  in the bulk of the tangle is almost homogeneous across the channel, while the vortex line density is not. Therefore the coefficient  $c_2^2$  has more complicated behavior, as is shown in Fig. 13. Nevertheless, when  $c_2^2$  is averaged over the core and near-wall regions separately, the closure Eq. (20) works quite well, especially at low  $T$ , as is shown in Appendix D, Fig. 24.

It turned out that the values of  $\mathcal{B}$  are very weakly dependent on the position in the channel. The difference between the values of  $c_2^2$  in the channel core and near the walls is compensated by the corresponding difference in the values of  $\mathcal{L}_0$ , such that  $\mathcal{B}$  is almost constant everywhere in the channel, with the exception of the immediate vicinity of the tangle edge, where the measurements of  $c_2^2$  become unreliable. To compare  $\mathcal{B}$  for various flow conditions, we plot in Fig. 18 its dimensionless form

$$\mathcal{B}^\dagger = \mathcal{B}\kappa/(V_{\text{ns}}^0)^2 \approx \alpha c_2^2 \Gamma^2, \quad (21)$$

where in the right-most relation we took into account [39] that  $\ln(R/a_0)/(4\pi) \approx 1$  and  $\Gamma^2 = \kappa^2 \mathcal{L}_0/(V_{\text{ns}}^0)^2$  is a dimensionless coefficient relating [39] the steady-state homogeneous VLD and the counterflow velocity. The coefficient  $\mathcal{B}^\dagger$  is expected to be a rising function of the temperature, but to have only weak dependence on other flow conditions. The streamwise profiles of  $\mathcal{B}^\dagger$  are illustrated for  $T = 1.3$  K,  $U_c = 3$  cm/s [Fig. 18(a)] and  $T = 1.9$  K,  $U_c = 1$  cm/s [Fig. 18(b)]. The values of  $\mathcal{B}^\dagger$  averaged over tangle bulk are summarized in Fig. 18(c). As expected, the coefficients  $\mathcal{B}^\dagger$  grow with the temperature, but otherwise, despite some scatter, are almost independent of the flow conditions. Note that, in accordance with the behavior of

$c_2^2$ ,  $\mathcal{B}^\dagger$  is larger in the flow generated by the flattened  $V_n$  profile (diamonds), than in the flow, generated by the corresponding parabolic profile (circles), for similar  $V_s^0$ .

Using almost constancy of  $\mathcal{B}$  over entire tangle, we can associate  $\tau_{\text{dec}} \equiv (\mathcal{B})^{-1}$  with some characteristic time, in this case of the tangle decay, and further rewrite

$$\tilde{F}(L) = \frac{L}{\tau_{\text{dec}}}(C - L), \quad C = \frac{\mathcal{A}}{\mathcal{B}}. \quad (22)$$

In the steady-state homogeneous tangle,  $C = 1$ . Again, there is no *a priori* reason to expect that this relation will hold in the current situation. However, as is shown in Fig. 19, up to natural fluctuations,  $C \approx 1$  along all the tangle including front regions, with accuracy about 20%–30% depending on the stage of the tangle development. In particular, at  $T = 1.3$  K the near-wall regions are more dissipative than the channel core, while at high  $T$  they are less dissipative. The closeness of the ratio  $C$  to unity indicates that we correctly account for all the relevant contributions to the  $\tilde{F}(L)$  in Eq. (18).

### E. Solution of VLD equation of motion

Having defined the functional form for  $\tilde{F}(L)$  and taking, for now,  $C = 1$ , we can return to Eq. (17) and rewrite it as

$$\begin{aligned} \partial_t L^j(x, t) + V_s^x \partial_x L^j(x, t) \\ = \tilde{D}^j \partial_{x,x} L^j(x, t) + 1/\tau_{\text{dec}} L^j(x, t)[1 - L^j(x, t)]. \end{aligned} \quad (23)$$

We now switch to dimensionless variables (omitting for shortness the index  $j$ )

$$\tau = t/\tau_{\text{dec}}, \quad l = x/\sigma, \quad \sigma = \sqrt{\tilde{D}\tau_{\text{dec}}}, \quad (24)$$

$$w = V_s^x/V_{\text{diff}}, \quad V_{\text{diff}} = \sigma/\tau_{\text{dec}}, \quad (25)$$

to rewrite Eq. (23) as

$$\partial_\tau L^j + w^j \partial_l L^j = \partial_{l,l} L^j + L^j - (L^j)^2. \quad (26)$$

Comparing with Eq. (5), we see that Eq. (26) is the ARD equation of FKPP type for the vortex line density, which for front velocities  $v_f > 2\sqrt{\tilde{D}/\tau_{\text{dec}}}$  admits a traveling wave solution  $\zeta = c(l - V_f \tau)$  with the dimensionless front speed  $V_f = v_f/V_{\text{diff}}$ . Substituting this solution to (26), we get an equation that defines the velocity and the shape of the

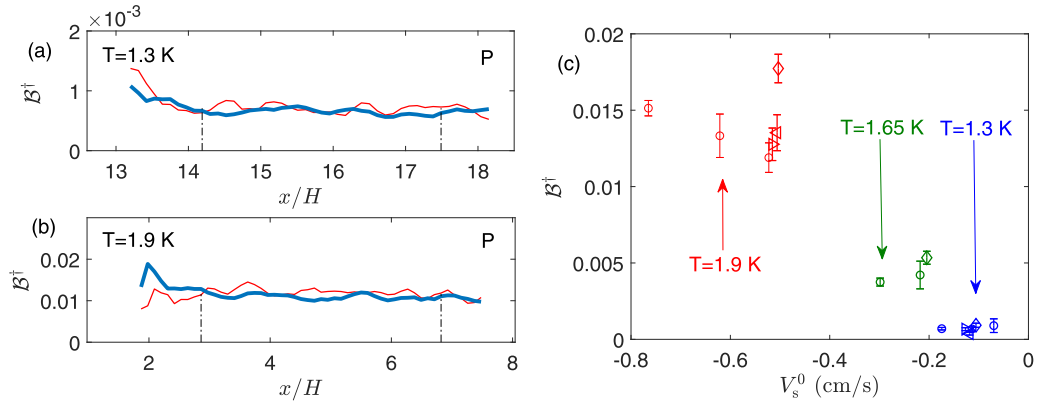


FIG. 18. The coefficient  $B^\dagger$  for various conditions. Streamwise profiles for (a)  $T = 1.3$  K,  $U_c = 3$  cm/s and (b)  $T = 1.9$  K,  $U_c = 1$  cm/s. Thin red lines correspond to the core profiles, thick blue lines denote near-wall profiles. Vertical dot-dashed lines mark the edges of the tangle bulk. In calculation of  $B$  for the core and for the walls regions we used the corresponding instantaneous values of  $\beta$ ,  $c_2^2$  and  $\mathcal{L}_0$  and then averaged over time. (c)  $B^\dagger$  averaged over tangle bulk. Symbols, denoting various flow conditions, are the same as in Fig. 15.

front:

$$[c_j v^j \partial_\zeta + c_j^2 \partial_{\zeta, \zeta}] L^j + L^j - (L^j)^2 = 0, \quad v^j = V_f^j - w^j. \quad (27)$$

A similar equation was obtained by Nemirovskii [15] for 1D front propagation, using the original Vinen's form for  $F(L) = \alpha_{Vi} L^{3/2} - \beta_{Vi} L^2$ , and solved numerically for the front speed, with the parameters estimated for the homogeneous steady-state vortex tangle by Schwarz [16] and the diffusion constant [54]  $D \approx 2.2\kappa$ .

Equation (27) may be solved analytically using Tahn method [55,56]. A general form of these solutions, symmetric with respect to the direction of propagation, reads

$$L(\zeta) = \frac{1}{4} [1 \pm \tanh \zeta]^2, \quad c = \frac{1}{2\sqrt{6}}, \quad v = \mp \frac{5}{\sqrt{6}}, \quad (28)$$

or, relaxing the requirement that  $\mathcal{C} = 1$ ,

$$L(\zeta) = \frac{\mathcal{C}}{4} [1 \pm \tanh \zeta]^2, \quad c = \frac{\sqrt{\mathcal{C}}}{2\sqrt{6}}, \quad v = \mp \frac{5\sqrt{\mathcal{C}}}{\sqrt{6}}, \quad (29)$$

Returning to the original dimensional variables

$$L(x) = \frac{1}{4} \left[ 1 \pm \tanh \left( \frac{1}{\lambda} [x - v_f t] \right) \right]^2, \quad (30)$$

$$\lambda = 2\sigma\sqrt{6/\mathcal{C}}, \quad v_f = \pm 5 V_{\text{diff}} \sqrt{\mathcal{C}/6} + V_s^x, \quad (31)$$

where  $\lambda$  is the front width. As we can see, the effective diffusion constant and the characteristic decay time define both the front width and the front velocity via the diffusion spread  $\sigma$  and its speed  $V_{\text{diff}}$ .

The similar (symmetric) solution was postulated in Ref. [13] without derivation, assuming  $F(L)$  based on Vinen's form of  $F(L)$  for the case of thermal counterflow [6] in the presence of a wall.

However, as we know now, the hot and cold fronts are of different types. Strictly speaking, only hot fronts are of FKPP type (pulled) and fulfill the underlying assumptions for the solution. Nevertheless, we may hope that, at least at high temperatures, the solution will describe reasonably well also the cold fronts.

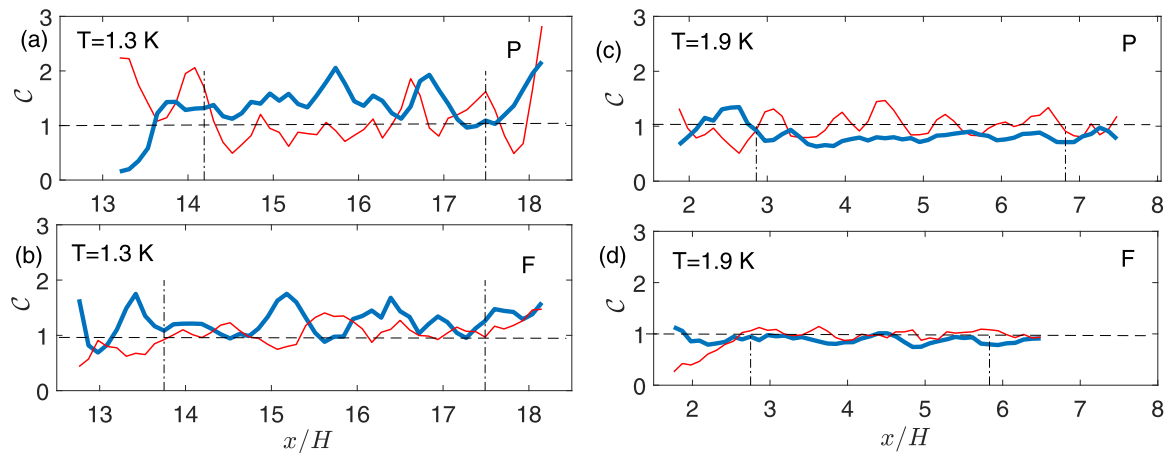


FIG. 19. The ratio  $\mathcal{C}$  for various conditions. The profiles for the parabolic  $V_n$  with (a)  $T = 1.3$  K,  $U_c = 3$  cm/s and (c)  $T = 1.9$  K,  $U_c = 1$  cm/s. The profiles of  $\mathcal{C}$  for the corresponding flattened profiles are shown in (b) for  $T = 1.3$  and (d) for 1.9 K. Thin red lines correspond to the core profiles, thick blue lines denote near-wall profiles. Vertical dot-dashed lines mark the edges of the tangle bulk. Horizontal dashed lines mark the value  $\mathcal{C} = 1$ .

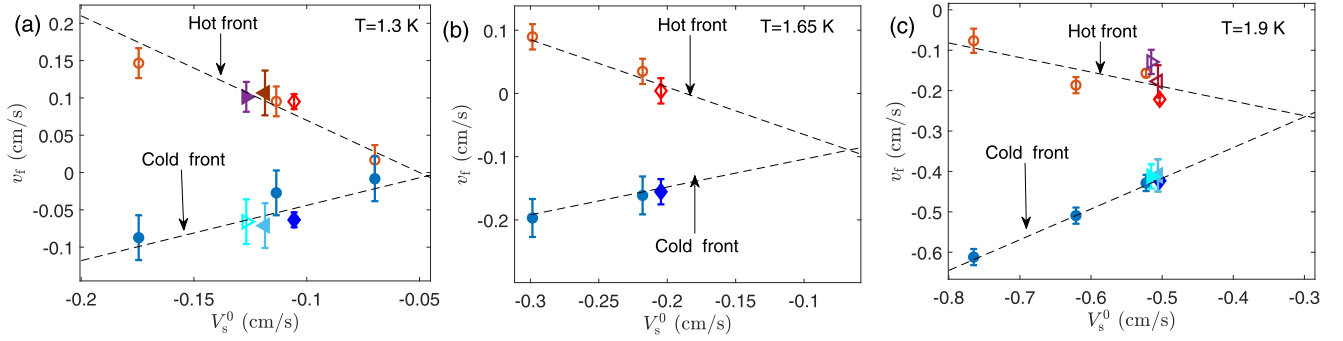


FIG. 20. Front velocities as a function of mean superfluid velocity for (a)  $T = 1.3$ , (b)  $1.65$ , and (c)  $1.9$  K. In all panels, different flow conditions are represented by different symbols:  $\circ$  denote front velocities for the parabolic  $V_n$  and various  $U_c$ ,  $\diamond$  corresponds to the flattened  $V_n$  profile,  $\triangleright$  and  $\triangleleft$  denote channel width  $H = 0.15$  and  $0.2$  cm, respectively. The symbols, marking cold front velocities, are filled, the symbols for the hot front velocities are empty. Dashed lines serve to guide the eye only.

Recalling that  $\tilde{D}$  depends on the flow conditions and therefore may be different for the channel core and near the walls, we get solutions for four fronts:

$$L^{j,c}(x) = \frac{1}{4} \left[ 1 + \tanh \left( \frac{1}{\lambda^{j,c}} [x - v_f^c t] \right) \right]^2, \quad (32)$$

$$L^{j,h}(x) = \frac{1}{4} \left[ 1 - \tanh \left( \frac{1}{\lambda^{j,h}} [x - v_f^h t] \right) \right]^2, \quad (33)$$

where  $\lambda^{j,c}$ ,  $\lambda^{j,h}$  are the widths of the corresponding fronts and  $v_f^c$ ,  $v_f^h$  are the corresponding front velocities. Here a word of caution is in order. The solutions (32) and (33) do not describe any transient behavior, such as VLD hump in the channel core near the hot front, strong VLD fluctuations at the fronts at low  $T$ , or effects of the different type of the nonlinearity for the cold fronts. Since fronts of the studied tangles most probably did not reach the expected limiting shapes, all parameters are considered as effective and corresponding to the chosen time  $t_f$ .

The mean front shapes were calculated using the procedure described in Appendix C and fitted with the solutions (32) and (33) to obtain the front velocities  $v_f^h$ ,  $v_f^c$  and front widths  $\lambda^{j,c}$ ,  $\lambda^{j,h}$ .

### F. Front velocities and shapes

The front speeds are shown in Fig. 20 as a function of the mean superfluid velocity  $V_s^0$ . It is clearly seen that  $v_f$  depends linearly on the advection velocity, with hot and cold front speeds having opposite trends, independent of the actual orientation of the hot front velocity. All data for a given temperature are well fit by the same linear dependence, shown as black dashed lines. Note that the front velocities are the same for the channel core and the near-wall regions. This point requires additional attention. As we mentioned earlier, the hot front is lead by the channel core, while the cold front is defined by the near-wall region. Moreover, the superfluid velocity in the bulk of the channel, as we showed in Fig. 8, is close to the corresponding  $v_f$ . This raises a natural question, how the hot front velocity near the channel walls becomes equal to that in the core and similarly, the cold front velocity in the core becomes equal to  $v_f^c$  near the channel walls? The answer lies in the action of the transverse flux  $\partial \mathcal{J}_y^j(x, t) / \partial y$

that changes very strongly in the fronts regions, but is almost constant along the tangle, see Fig. 26 and Appendix D. In this way, the hot front near the wall is formed by VLD brought by the flux from the channel core and its velocity matches the velocity at the core only very close to the tangle edge. Similarly, the superfluid velocity in the core of the channel is quickly changed to  $v_f^c$  by the transverse flux which in this region brings VLD from the walls toward the channel core. Here, the flux is much weaker than in the hot front region and the development of the cold front in the channel core is a result of a complicated interplay of various mechanisms, leading to long-lasting transient behavior.

At low  $T$ ,  $|v_f^h| > |v_f^c|$  for the same advection velocity  $V_s^0$ , while at high  $T$  the relation is opposite. This observation is in agreement with the early experiments in thin capillaries [7,8]. Moreover, the front velocities, observed in Ref. [8] for  $T = 1.34$  K at low heat fluxes, are similar to  $v_f$  measured in our simulations at  $T = 1.3$  K. The linear dependencies point out to a particular value of  $V_s^{0,*}$  at which the front speeds are expected to be the same. It is natural to associate the corresponding  $v_f^*$  with the onset of the front solution in the counterflow, for instance, to the formation of narrow structures similar to the puffs in the classical pipe flow with two fronts moving with the same velocity. Since without advection flow (or more specifically, the counterflow  $V_{ns}$ ), the counterflow turbulence does not exist, the onset front velocity  $v_f^* > v_0$ . Note that at all temperatures, the values of  $V_s^{0,*}$  are larger than the critical  $V_{s,c}^0$ , below which the vortex tangle is not formed. The values of  $V_s^{0,*}$  were estimated from the critical counterflow velocity  $v_c$  obtained by fitting  $\sqrt{\mathcal{L}_0} = \Gamma(V_{ns} - v_c) / \kappa$ , and the counterflow condition. The onset front velocities  $v_f^*$  and  $V_s^{0,*}$  are listed in the Table III.

TABLE III. Onset front velocities  $v_f^*$  and corresponding mean superfluid velocities  $V_s^{0,*}$ . The error bars reflect the sensitivity of the linear fitting procedure.

$T$ , K	1.3	1.65	1.9
$v_f^*$ , cm/s	$-0.005 \pm 0.02$	$-0.09 \pm 0.02$	$-0.26 \pm 0.02$
$V_s^{0,*}$ , cm/s	$-0.05 \pm 0.02$	$-0.07 \pm 0.02$	$-0.30 \pm 0.02$



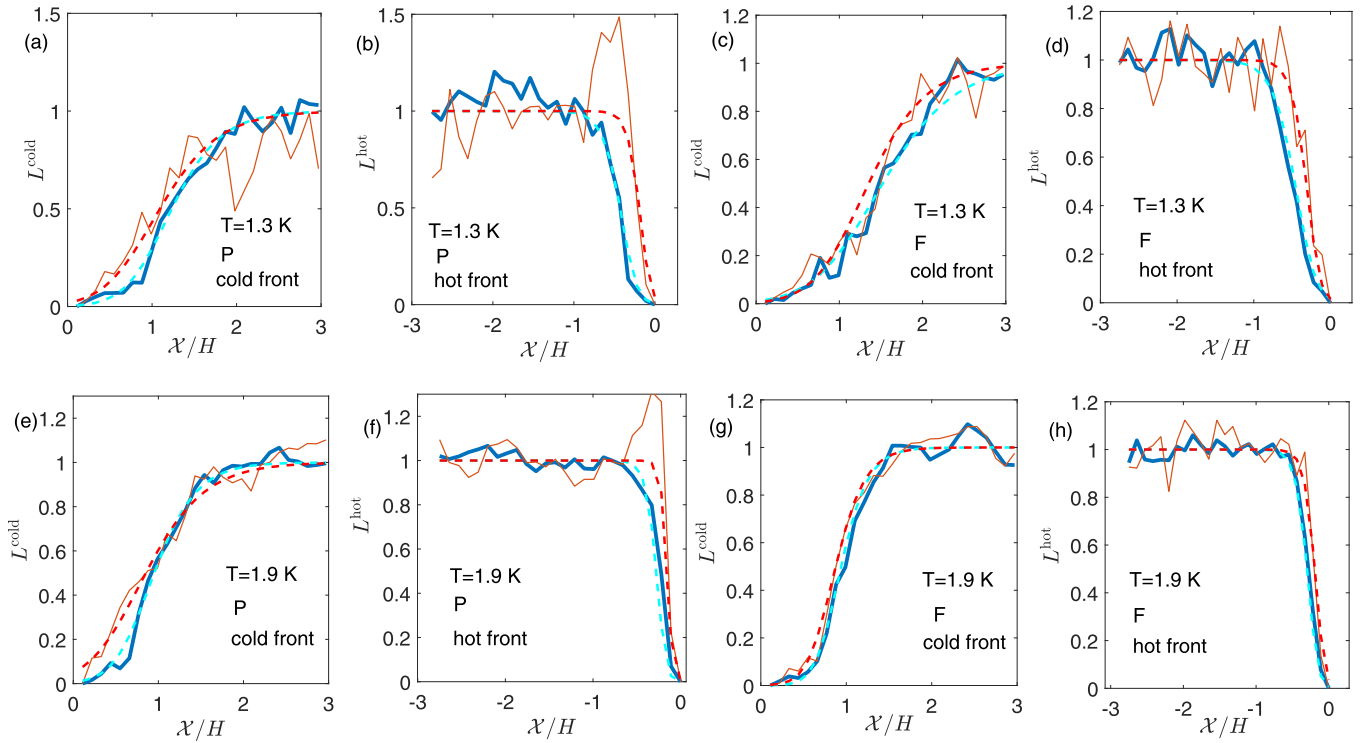


FIG. 21. The cold and hot fronts shapes for various conditions: [(a) and (b)]  $V_n$  with  $T = 1.3$  K,  $U_c = 3$  cm/s; [(c) and (d)]  $T = 1.3$  K and flattened  $V_n$  profile; [(e), (f)]  $T = 1.9$  K,  $U_c = 1$  cm/s; and [(g) and (h)]  $T = 1.9$  K and flattened  $V_n$  profile. The cold front shapes are shown in (a), (c), (e), and (g), the hot front shapes are shown in (b), (d), (f), and (h). Thin red lines correspond to the core fronts, thick blue lines denote near-wall fronts. Cyan dashed lines denote fits for the near-wall fronts, red dashed lines denote fits for the fronts in the channel core.

The representative front shapes, together with their fits by the solutions (32) and (33), are shown in Fig. 21. The horizontal axis shows the distance from the front edge ( $\mathcal{X} = 0$ ) for the core and the near-wall regions separately. First of all, we note the presence of the narrow VLD hump, localized between the tangle bulk and the hot front in the tangles driven by the parabolic  $V_n$  profiles, Figs. 21(a) and 21(c). This hump is not formed when the normal-fluid velocity profile is flattened, Figs. 21(b) and 21(d). In all cases, the hot fronts are 2–5 times more narrow than the cold fronts. The hot fronts are steeper in the core of the channel than near the walls, while cold fronts are steeper near the walls, or similar. The presence of a shallow shoulder at small  $L$  in the cold front shapes, well seen for the near-wall front shapes at both temperatures, is a sign of non-FKPP nonlinearity and is not accounted for by the solution. However, the solution (32) describes reasonably well the overall cold front shapes, especially at high temperatures, at which the fronts are well-formed and developed.

### G. Effective diffusivity

The importance of the diffusion mechanism for the decay of inhomogeneous tangle was studied theoretically [54] and numerically [57–59] for the decaying tangles at  $T = 0$  K with most recent estimates of the effective diffusion constant in the range  $(0.1 - 1)\kappa$ . The presence of dissipative walls reduces [58] the values of the effective diffusion constant, while in the 3D unbounded vortex tangle [59] the value of the effective diffusion constant was found to be close to  $0.5\kappa$ .

Using the relation between the front width and the effective diffusion constant, Eqs. (24) and (31), we can estimate  $\tilde{D}$  for various conditions. For that, we rewrite Eq. (31) as

$$\tilde{D}^{j,c} = \frac{(\lambda^{j,c})^2}{24\tau_{\text{dec}}}, \quad \tilde{D}^{j,h} = \frac{(\lambda^{j,h})^2}{24\tau_{\text{dec}}}, \quad (34)$$

where we retain  $\mathcal{C} = 1$  and  $\tau_{\text{dec}} = \text{Const.}$  for given conditions. To get an idea of what behavior to expect from  $\tilde{D}$  we rewrite (34) (omitting indices  $j$ ,  $c$ , and  $h$  for clarity) as

$$\tilde{D} = \frac{\lambda^2 \mathcal{B}}{24} = \frac{\lambda^2 \mathcal{B}^\dagger (V_{\text{ns}}^0)^2}{24\kappa}. \quad (35)$$

The temperature dependence of  $\tilde{D}$  is therefore mostly defined by  $\mathcal{B}^\dagger$ , the dependence on the driving velocity by  $(V_{\text{ns}}^0)^2$  and the influence of other flow conditions, including the spatial dependence—by the front width  $\lambda$ . There is no systematic dependence of the front width on the driving velocity. Recall that the cold fronts are wider than the hot fronts, such that for the given  $T$  and  $V_{\text{ns}}^0$ ,  $\tilde{D}^{j,c} > \tilde{D}^{j,h}$  with the difference reaching up to an order of magnitude. The typical front width range decreases with temperature, such that  $\lambda^c \sim (0.05 - 0.1)$  cm at  $T = 1.3$  K, while at  $T = 1.9$  K,  $\lambda^c \sim (0.03 - 0.05)$  cm. The hot fronts are more narrow:  $\lambda^h \sim (0.02 - 0.05)$  cm at  $T = 1.3$  K, while  $\lambda^h \sim (0.005 - 0.03)$  cm at  $T = 1.9$  K. On the other hand,  $\mathcal{B}^\dagger$  grows with  $T$ . As a result, for the studied range of flow conditions, at the cold front, the typical values are  $\tilde{D}^c \sim (0.5 - 1.5)\kappa$ , while at the hot fronts  $\tilde{D}^h \sim (0.01 - 0.1)\kappa$  and are larger for higher temperatures. This  $T$  dependence is more prominent for the flows driven by the

TABLE IV. Effective diffusivity at the cold (c) and hot (h) fronts near the wall and in the channel core for representative conditions. P and F denote the parabolic and the flattened  $V_n$  profile, respectively. The error-bars account for  $\mathcal{C} = 1 \pm 0.2$  as well as the errors in measurements of  $\lambda$  and  $\mathcal{B}$ . The flow conditions are the same as in Figs. 13 and 14.

Type $V_n(y)$	$T = 1.3$ K		$T = 1.65$ K		$T = 1.9$ K	
	P	F	P	F	P	F
$\bar{D}^{\text{core,c}}/\kappa$	$0.5 \pm 0.2$	$1.4 \pm 0.5$	$0.7 \pm 0.3$	$1.1 \pm 0.3$	$1.3 \pm 0.4$	$1.3 \pm 0.3$
$\bar{D}^{\text{wall,c}}/\kappa$	$0.4 \pm 0.1$	$1.0 \pm 0.5$	$0.8 \pm 0.3$	$0.7 \pm 0.2$	$1.3 \pm 0.3$	$1.3 \pm 0.3$
$\bar{D}^{\text{core,h}}/\kappa$	$0.01 \pm 0.005$	$0.02 \pm 0.01$	$0.06 \pm 0.02$	$0.05 \pm 0.02$	$0.04 \pm 0.01$	$0.08 \pm 0.02$
$\bar{D}^{\text{wall,h}}/\kappa$	$0.03 \pm 0.01$	$0.12 \pm 0.04$	$0.05 \pm 0.02$	$0.11 \pm 0.01$	$0.20 \pm 0.05$	$0.32 \pm 0.07$

parabolic normal-fluid velocity. The representative values of  $\bar{D}$ , calculated according to Eq. (34), are listed in Table IV. It is important to remember that the effective diffusivity  $\bar{D}$  is not a material property of superfluid  $^4\text{He}$ , but a dynamical property of propagating fronts in the particular flow conditions, including different nonlinear processes in the front regions. In addition, the values listed in the table correspond to the reached stage of the tangle development and are sensitive to the presence of the transient processes in the tangle core. Nevertheless, since the order of magnitude of  $\bar{D}$  is the same for the flows driven by the parabolic and by flattened  $V_n$  profiles at all studied temperatures, these values may be considered as a robust dynamical property of the propagating fronts in the channel counterflow.

The values of  $\bar{D}$  at the hot front are remarkably close to the values of the effective diffusion constant found numerically in the bounded [57,58] and unbounded [59] bulk tangles at zero temperature. We do not have a reliable measure of the diffusion in the bulk of the tangle. However, since the values of many of the tangle properties in the bulk are similar to those in the hot front region, we suggest that also the values of  $\bar{D}$  in the tangle bulk would be similar to those in the hot front region at least in the order of the magnitude.

#### IV. DISCUSSION

Our simulations of the quantum vortex tangles that develop freely in the channel from localized initial conditions under the influence of the counterflow velocity, give a unique insight into their natural dynamics and structure. Despite a wide variety of the flow conditions experienced by the vortex lines that influence the local dynamics, there are many common features.

In particular, the tangles may be divided into regions according to their dynamics. The regions near the tangle edges exhibit front dynamics. The dynamics of tangle bulk is more similar to that of the steady-state stationary tangles. In the bulk, the parts of the tangle that develop near the channel wall, are first to reach equilibrium VLD and grow almost symmetrically with respect to the direction of the counterflow velocity. On the other hand, the transient tangle dynamics in the channel core is slower, with notable asymmetry and preferential growth of VLD toward the hot front, resulting in the long-lasting streamwise inhomogeneity. This behavior is similar at high and low temperatures, despite the different direction of the hot front propagation. This asymmetry is originated from the production of the vortex line length, strongly peaked in the

channel core within the hot front region. The only difference between the dynamics at different velocities of the driving normal fluid and even its wall-normal profile is the duration of the transient behavior and degree of the inhomogeneity of resulting vortex tangle. Conversely, the structural properties of the vortex tangle, such as the ratio between the curvature and the vortex line density and preferential orientation of the local velocity, reach their steady-state distributions as soon as the tangle become three-dimensional, with core values similar to those obtained in the simulations of the steady-state vortex tangles and the experimental estimates.

The VLD is higher near the walls than in the channel core, peaking at about the intervortex distance, in agreement with the results of simulations of steady-state tangles in the channel. This difference between the channel core and the near-wall regions is less prominent when the flow is driven by the normal-fluid velocity with the flattened profile. A similar trend of relatively flat VLD distribution in the channel core, that extends towards the walls, was observed in simulations with wider channels at all temperatures.

An explicit account for the advection mean superfluid velocity allowed us to detect a superfluid motion of various scales within the vortex tangle. The largest scales of this motion reach the channel size at strong driving velocity. When normal-fluid velocity profile is flattened, as is expected in the turbulent flow, superfluid motions exist at many scales. The presence of this large-scale superfluid motion is reflected in the streamwise inhomogeneity of various tangle properties. The typical period of the fluctuations is of the order  $H/2$ , corresponding to the largest eddies formed in the tangle.

The analysis of the dynamics of the fronts in the framework of the advection-diffusion-reaction equation gives unexpected results. The two fronts are driven by different parts of the flow and have a different type of nonlinearity of the generalized production term. The hot fronts are *pulled*, i.e. driven by the flow in the channel core and the leading edge dominate in defining their high steepness and the propagation speed. The cold fronts, on the other hand, are lead by the near-walls tangle and are *pushed* by the nonlinear interior. A low-density foot moves before the tangle, and only at about a quarter of the front width, the VLD start to rise fast. These fronts are wide and the shape difference between the channel core and near the walls is larger. In accordance with ADR dynamics, the front velocities are linearly proportional to the advection mean superfluid velocity, with common dependence for all conditions at a given temperature. Unlike the classical pipe flows, where the downstream front of the puffs and slugs

(corresponding to the cold front in the counterflow) always move faster [36,37] than the upstream front (corresponding to the hot front in the counterflow), in the  $^4\text{He}$  counterflows, the relation between the two fronts velocities depend on the temperature. In particular, in the classical flow, the magnitude of the upstream front velocity always decreases with the increasing velocity of the bulk flow. In the counterflow, such behavior of the hot front is observed only at high temperatures. At low  $T$ , it is the hot front that becomes faster for higher heat fluxes. The possible reason for such a difference is the opposite orientation of the mean superfluid velocity in the channel core and near the walls at low  $T$ . Therefore, at these conditions, the notion of the downstream direction becomes local and the dynamics of vortex tangles is more complicated than that of the slugs in the classical pipe flow.

The analytic solution of the equation of motion (17) fits well the overall front shapes for all conditions, while it does not describe the transient effects near the hot fronts and the effects of the non-FKPP nonlinearity at the cold fronts. These solutions allow extracting the effective diffusivity which is flow-dependent and different at the hot and at the cold fronts. The values of the effective diffusivity measured at the hot fronts agree in the order of magnitude with recent estimates from simulations at  $T = 0$  K.

Although the current study ignores the back-reaction of the superfluid component on the dynamics of the normal fluid, we expect that in the studied range of flow parameters most of the influence is captured by the flattening the laminar normal-fluid velocity profile. Other effects may include changes in the duration of the transient regimes.

Among questions that can only be answered when both components are fully coupled, are how the presence of the vortex tangle in the superfluid component influences the transition of the normal-fluid component from the laminar to the turbulent state (so-called TI-TII transition) and whether at sufficiently large heat fluxes the transition to turbulence may occur simultaneously in both components.

## APPENDIX A: A GUIDE TO MAIN NOTATIONS

In this Appendix, we collect the main notations used in the paper. The notations are grouped by their physical meaning and organized following the structure of the paper. The references to the relevant sections, equations, and tables are included for convenience.

- (1) Physical properties of  $^4\text{He}$ , see Sec. II A and Table I:
  - (i)  $\rho, \rho_n(T), \rho_s(T)$  – the density of  $^4\text{He}$  and the temperature-dependent partial densities of the normal-fluid and superfluid components;
  - (ii)  $a_0 = 1.3 \times 10^{-8}$  cm – the core radius of the vortex lines;
  - (iii)  $\kappa = 9.97 \times 10^{-4}$  cm<sup>2</sup>/s – the circulation quantum;
  - (iv)  $\alpha(T), \alpha'(T)$  – temperature-dependent mutual friction parameters, see Eq. (1);
- (2) Coordinate systems and characteristic lengths:
  - (i) The Cartesian coordinate system in the channel ( $x, y, z$ ) – the streamwise, wall-normal and spanwise directions, respectively, see Sec. II B and Fig. 1;
  - (ii)  $s(\xi)$  – The Cartesian coordinate of the vortex line, parameterized with the arc-length  $\xi$ ;

- (iii) The coordinate system associated with the vortex line point  $s(\xi)$ :  $s' \equiv ds/d\xi$  – the local direction of the vortex line;  $s'' \equiv d^2s/d\xi^2$  – the local curvature vector;  $(s' \times s'')$  – the local binormal vector;

- (iv)  $\ell$  – the typical distance between vortex lines in the tangle;

- (v)  $H$  – the channel width.

(3) Various velocities:

- (i)  $V_n, V_s, V_{ns}$  – the macroscopic normal-fluid, superfluid, and counterflow velocities, see Sec. II A;

- (ii)  $U_c$  – the value of the centerline velocity of the parabolic normal-fluid velocity profile;

- (iii)  $V_s^0, V_{loc}, V_{nl}$  – the mean, local and nonlocal contributions to the superfluid velocity  $V_s, V_{mf}$  – the contribution to the vortex line velocity due to the interaction with the normal fluid,  $V_{drift}$  – full velocity of the vortex line, see Eq. (1), Secs. II B and III B;

- (iv)  $V^\dagger = V/V_{ns}^0$  – the normalized velocities are used to compare various flow conditions. The mean counterflow velocity  $V_{ns}^0$  is defined using the zero-mass-flux condition, Eq. (4), see also Table II.

(4) Division of the vortex tangle into regions, for details see Appendix B:

- (i) in the streamwise direction – the cold front, moving in the direction of the mean superfluid velocity, the tangle bulk, and the hot front, moving in the direction of the mean normal-fluid velocity;

- (ii) in the wall-normal direction – the core of the channel and two near-wall regions.

(5) Vortex tangle properties:

- (i)  $\mathcal{L}(\mathbf{r}) \equiv \int_{\Omega'} ds/V'$  – the vortex line density (VLD), the length of the vortex lines configuration  $\Omega'$  in a physically small volume  $V'$ , see Secs. II C, II D;

- (ii)  $\mathcal{L}_0$  – the mean value of VLD averaged over the tangle bulk in the channel core or the near-wall regions, see Table II; The intervortex distance in the corresponding region is defined as  $\ell = (\mathcal{L}_0)^{-1/2}$ ;

- (iii)  $\mathcal{L}^\dagger = \mathcal{L}\kappa^2/(V_{ns}^0)^2$  – the dimensionless VLD is used to compare various flow conditions;

- (iv)  $L = \mathcal{L}/\mathcal{L}_0$  – the normalized VLD is used to solve the equation of motion for the tangle fronts;

- (v) Structural properties of the tangle:

- $\varkappa \equiv |s''|$  – the local curvature of the vortex line;

- $\langle \varkappa^2 \rangle = \int_{\Omega'} |s''|^2 ds/V'$  – the mean square curvature;

- $c_2$  – compares the root-mean-square radius of curvature with the mean intervortex distance, appears in the theory as  $c_2^2 = \langle \varkappa^2 \rangle / \mathcal{L}$ , see Secs. II G, III D and Appendix D;

- $I_{\ell,x}$  – the streamwise projection of the local bi-normal vector defines the major contribution to the vortex line length production. Its dimensionless index  $I_{\ell,x}^\dagger = I_{\ell,x}/|s''|$  quantifies the orientation of the local vortex line velocity with respect to the direction of the counterflow, see Sec. II G and Appendix D;

(6) Advection-reaction-diffusion description of the front propagation – the history, see Sec. III A:

- (i)  $0 < \theta < 1$  – the propagating quantity;

- (ii)  $\mathbf{u}(\mathbf{r}, t)$  – the advection velocity;

- (iii)  $D$  – the diffusivity; If  $\mathbf{u}(\mathbf{r}, t) \neq 0$ , the diffusion is characterized by the effective diffusion constant  $D_{\text{eff}}$ .

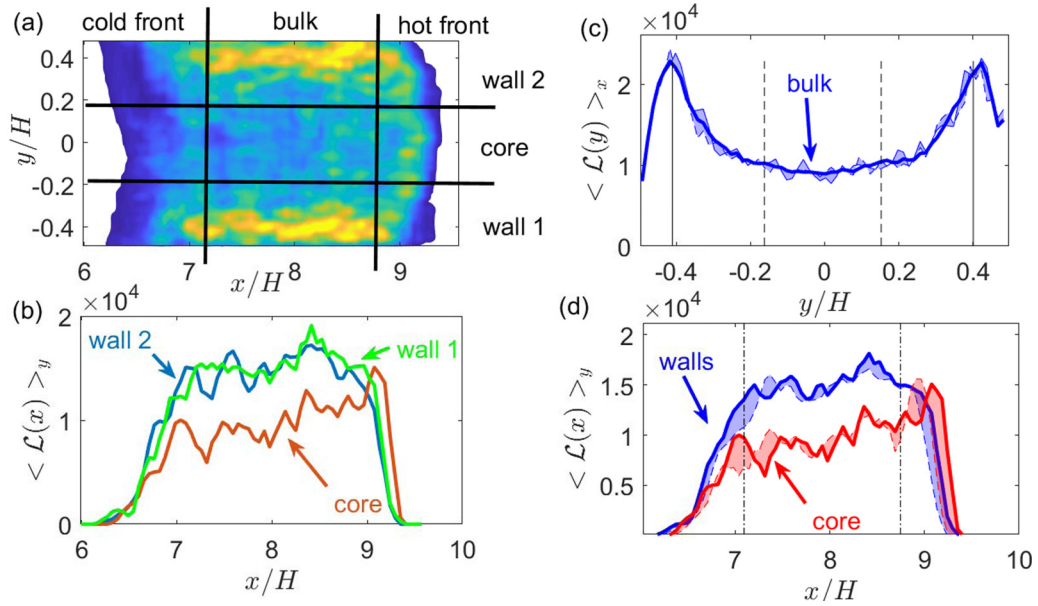


FIG. 22. Schematic representation of various averaging zones. (a) 2D map of  $\mathcal{L}(x, y)$  ( $\text{cm}^{-2}$ ) in which various averaging zones are marked. (b) Streamwise profiles  $\langle \mathcal{L}(x) \rangle_y$  averaged over two near-wall zones and over the core in the  $y$  direction. (c) The wall-normal profile  $\langle \mathcal{L}(y) \rangle_x$  averaged over the tangle bulk in the  $x$  direction. (d) The streamwise profiles  $\langle \mathcal{L}(x) \rangle_y$ , in which two near-wall zones are averaged together. In (c) and (d), the shaded area shows variation of VLD between  $t_f - t_{\text{av}}$  (thin dashed lines) and  $t_f$  (thick solid lines).

(iv)  $F(\theta)$  – the nonlinear reaction term. If the maximum slope of  $F(\theta)$  occurs at  $\theta = 0$ , the fronts are called *pulled* fronts and their dynamics is fully determined by the region  $\theta \approx 0$ . When the maximum slope of  $F(\theta)$  occurs at  $\theta > 0$ , the front is *pushed* by the non-linear interior;

(v)  $v_0$  – the speed of the front, defined by the marginal stability criterion;  $v_{\min} \geq v_0$  – the minimal front velocity in the presence of advection;  $v_f \geq v_{\min}$  – the actual speed of the front;

(7) The equation of motion for VLD, see Secs. III B, III C, III D:

(i) The equation of motion for  $L$ , Eq. (8), is the 2D ARD-type equation with the VLD flux  $\mathcal{J}$ , the effective VLD diffusivity  $\tilde{D}$  and the production term  $F(L)$ ;

(ii) Averaged separately for the channel core and the near-wall regions, it becomes a set of two 1D equations Eq. (17) in which the advection term  $\partial \mathcal{J} / \partial x$  and the production term  $\tilde{F}(L)$  are modified to include the contributions from the streamwise tangle-induced VLD flux  $\partial \tilde{J}_x / \partial x$  and the transverse VLD flux  $\partial J_y / \partial y$ , respectively;

(iii) The proposed closure for  $\tilde{F}(L) = \mathcal{A}L - \mathcal{B}L^2$  is based on the nonlinearity type in the hot front region. The coefficient  $\mathcal{B} = -\alpha(\kappa/4\pi) \ln[(\chi)a_0]c_2^2\mathcal{L}_0$  plays an important role of the characteristic frequency of the tangle decay  $\tau_{\text{dec}} = (\mathcal{B})^{-1}$ . It is almost constant over most of the tangle for the given conditions, as well as the ratio  $\mathcal{C} = \mathcal{A}/\mathcal{B} \approx 1$ , see Sec. III D and Eq. (22);

(iv) Various terms that contribute to  $\tilde{F}(L)$ , i.e.  $\mathcal{P}_1, \mathcal{P}_2, \mathcal{P}_3, \mathcal{D}, \mathcal{J}$ , are defined in Eq. (10)–(16) and discussed in details in Appendix D.

(8) The solution of the equation of motion for VLD, see Secs. III E, III F and III G:

(i) The dimensionless Eq. (23) is formulated using the dimensionless variables based on the decay time  $\tau_{\text{dec}}$ , the

diffusion spread  $\sigma = \sqrt{\tilde{D}\tau_{\text{dec}}}$ , its velocity  $V_{\text{diff}} = \sigma/\tau_{\text{dec}}$  and the dimensionless front velocity  $V_f = v_s/V_{\text{diff}}$ ;

(ii) The solutions for the four front shapes  $L^{\text{core,c}}(x), L^{\text{wall,c}}(x), L^{\text{core,h}}(x), L^{\text{wall,h}}(x)$ , Eq. (32) and Eq. (33), involve the speeds of the cold and hot fronts  $v_f^c, v_f^h$  [Fig. 20] and the four widths of the corresponding fronts  $\lambda^{\text{core,c}}, \lambda^{\text{wall,c}}, \lambda^{\text{core,h}}, \lambda^{\text{wall,h}}$ ;

(iii) The values of the onset front velocities  $v_f^*$ , equal for the two fronts, and the corresponding  $V_s^{0,*}$  at which they are observed, are listed in Table III;

(iv) The four effective diffusion constants  $\tilde{D}^{\text{core,c}}, \tilde{D}^{\text{wall,c}}, \tilde{D}^{\text{core,h}}, \tilde{D}^{\text{wall,h}}$ , extracted from the fronts width according to Eq. (34), are listed in Table IV.

## APPENDIX B: CALCULATION OF VARIOUS PROFILES

The wall-normal and the streamwise profiles of various quantities are calculated according to the scheme shown in Fig. 22. The division into different zones is somewhat arbitrary, however, we have checked that the values of the tangle properties are robust with respect to the variation of the zones boundaries within two mesh sizes. For illustration, we use the vortex line density  $\mathcal{L}$ . The wall-normal profiles were obtained by averaging the 2D maps over the bulk region of the tangle defined at each time moment and further averaged over the last  $t_{\text{av}} = 0.2$  sec. The shading in Figs. 22(c) and 22(d) illustrates the variation between the profiles at time  $t_f - t_{\text{av}}$  (dashed lines) and  $t_f$  (solid lines). The streamwise profiles were calculated for  $t_f$  by averaging over the core and near-wall regions separately. In cases where the behavior at two near-wall regions was similar, they were averaged together. The streamwise profiles of structural properties, such as  $c_2^2$ , and various terms of the balance equation, in addition to averaging over the core and near-wall regions, were averaged over the last 0.1 s of

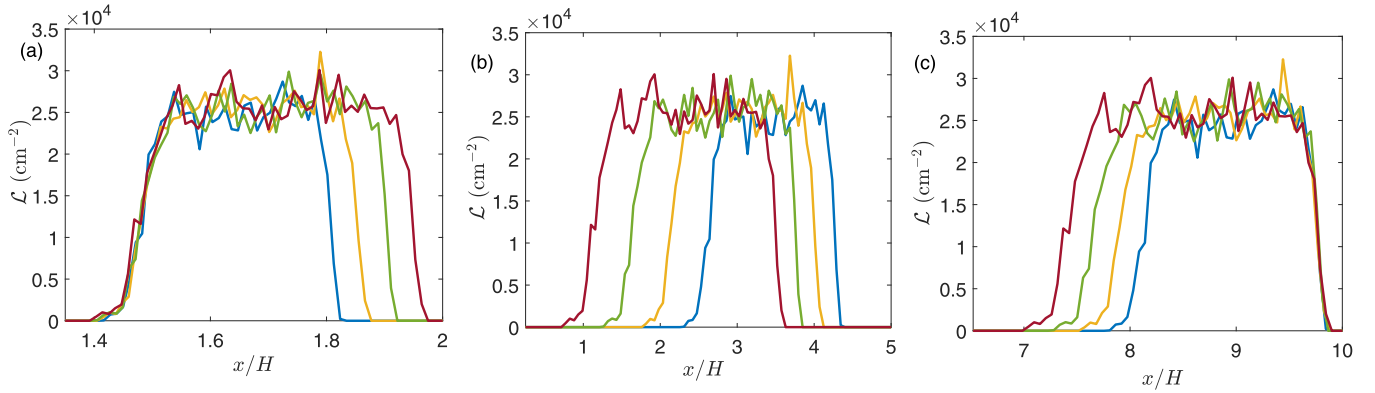


FIG. 23. The hot and cold front shapes. A series of streamwise VLD profiles corresponds to last 1 s of the evolution of the walls region,  $T = 1.9$  K, flattened  $V_n$ . (a) The profiles are collapsed using the cold front speed, (b) the original profiles, and (c) the profiles are collapsed using the hot front speed.

time evolution. In cases that involve division by  $\mathcal{L}$ , the points near the edge of the tangle, where  $\mathcal{L}(x) \approx 0$ , were omitted in calculation of the time average and not shown.

The intervortex distance  $\ell = \mathcal{L}^{-1/2}$ , shown in the wall-normal  $y$  profiles as vertical thin black lines, is calculated here at time  $t_f$  by averaging  $\mathcal{L}$  over bulk in  $x$  direction and over the near-wall region in  $y$  direction.

### APPENDIX C: FRONT SHAPE

The fronts of the tangles propagate without shape change. To show this, we shift the  $x$  positions of the streamwise VLD profiles  $\mathcal{L}(x)$ , corresponding to the time period when the bulk and the fronts are fully developed, to the left and to the right, such that the corresponding tangle edges overlap. This procedure is used to measure the front speeds  $v_f^c$  and  $v_f^h$  that allow such an overlap. The original profiles  $\mathcal{L}(x)$  are shown in Fig. 23(b). The result of the cold front collapse is plotted in panel (a) and of the hot front collapse in panel (c). Clearly, the front shape does not change during this time period. To obtain the front shape, we calculate the dimensionless VLD  $L = \mathcal{L}/\mathcal{L}_0$ , where  $\mathcal{L}_0$  is the mean VLD

in the bulk of the tangle. Since the values of VLD differ in the core of the channel and near the walls, we treat these regions separately. We further average these profiles over the time period of 0.2 s. In such a way we obtain four shapes, for the cold front and for the hot front in the core and in the near-wall regions, shown in Fig. 21. The same procedure was used to obtain the front shapes of other quantities of interest.

### APPENDIX D: TERMS OF THE BALANCE EQUATION

In this section, we provide a detailed description of various contributions to  $\vec{F}(L)$  used in the analysis of the front dynamics. As was shown in Sec. III D, the spatial distribution of the decay term  $\mathcal{D} \approx \alpha\beta c_2^2 \mathcal{L}_0 L^2$  essentially follows  $L^2$ . This representation faithfully describes the integral form (15) not only on average in the steady-state tangle but also locally and instantaneously, including the transient stage of the dynamics, as is shown in Fig. 24. To allow comparison, the dimensionless values  $\mathcal{D}^\dagger = \mathcal{D}\kappa/(V_{ns}^0)^2$  are plotted. The model slightly overestimates the decay term at high  $T$ , but otherwise should be considered very adequate everywhere

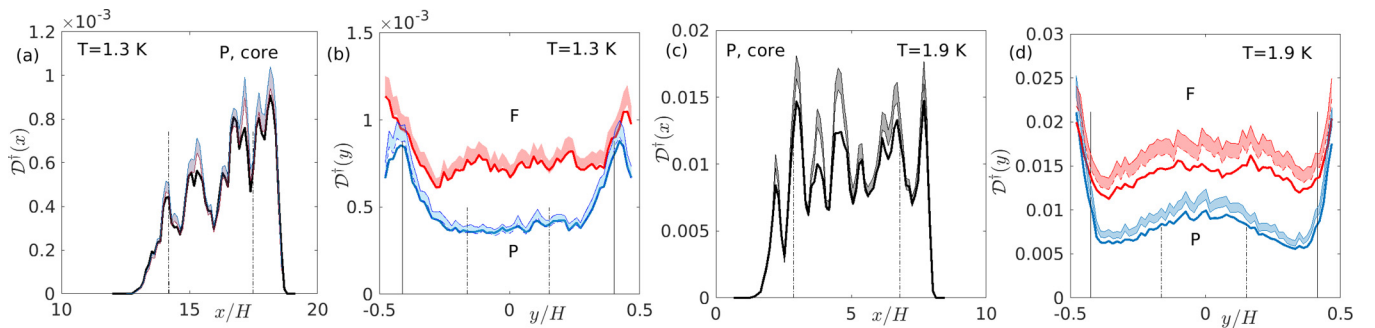


FIG. 24. The decay term Eq. (15) (thick lines) and its model form Eq. (20) with 95% confidence interval (shaded area) at different conditions. [(a) and (c)] The streamwise profiles for the channel core for (a)  $T = 1.3$  K, parabolic  $V_n$  with  $U_c = 3$  cm/s and (c)  $T = 1.9$  K, parabolic  $V_n$  with  $U_c = 1$  cm/s. [(b) and (d)] The wall-normal profiles for the conditions of (a) and (c), respectively, and matching flows with flattened  $V_n$  profile. Dot-dashed black lines mark the edges of the bulk and the core regions for the streamwise and for the wall-normal profiles, respectively. Thin solid lines in (b) and (d) are placed at the intervortex distance from the corresponding walls. The profiles are calculated as described in Appendix B. For normalization in Eq. (15),  $\mathcal{L}_0^{\text{core}}$  was used for the streamwise profiles in (a) and (c) and  $\mathcal{L}_0^{\text{wall}}$  for the wall-normal profiles in (b) and (d).

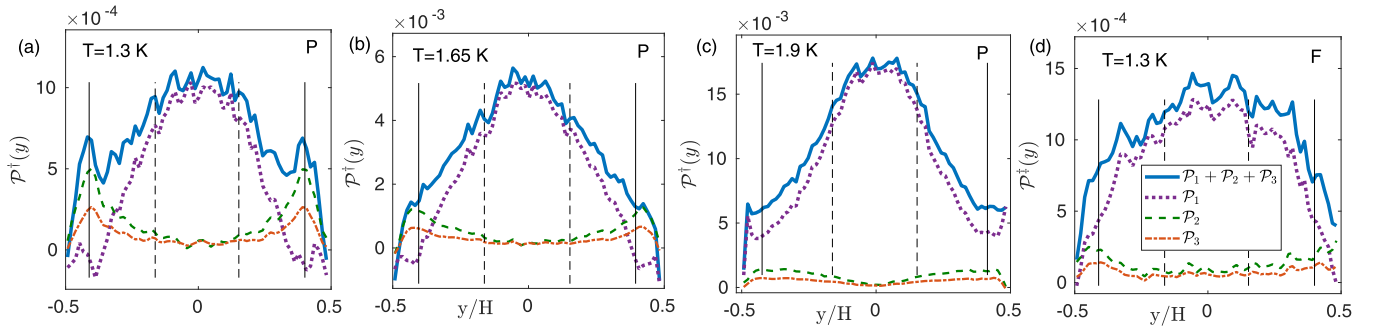


FIG. 25. The production terms:  $\mathcal{P}_1$  [Eq. (12), purple dotted line],  $\mathcal{P}_2$  [Eq. (13), green dashed line],  $\mathcal{P}_3$  [Eq. (14), brown dot-dashed line], and their sum (blue solid line) at different conditions. (a)  $T = 1.3$  K, parabolic  $V_n$  with  $U_c = 3$  cm/s; (b)  $T = 1.65$  K, parabolic  $V_n$  with  $U_c = 1.5$  cm/s; (c)  $T = 1.9$  K, parabolic  $V_n$  with  $U_c = 1$  cm/s and (d)  $T = 1.3$  K, flattened  $V_n$  profile. Dashed black lines mark the edges of the core region. Thin solid lines are placed at the intervortex distance from the corresponding walls.

in the tangle. Note that the strong streamwise inhomogeneity, amplified compared to VLD, is well reproduced by the model. The situation is different with the production term. Directly interpreting the model form as a product of average slowly varying fields, we get for  $\mathcal{P}_1 = \alpha \langle V_{ns,nl}^x \rangle \langle s' \times s'' \rangle_x L \approx \alpha V_{ns}^0 I_{\ell,x} L$ . So far, the problem of the closure for  $\mathcal{P}_1$  amounted to the question how to describe [6,16,29–31]  $I_{\ell,x}$  in terms of  $L$  and  $V_{ns}$ . As it follows from the discussion in Secs. IID and IIG, in the inhomogeneous flows, there is no simple answer to this question. Additional complication arises at low  $T$ , at which the contributions of  $\mathcal{P}_2 = \langle s' \cdot V_{nl}' \rangle L$  and  $\mathcal{P}_3 = -\alpha' V_{ns} \langle \varkappa \rangle L$  near the walls are not negligible. We do not attempt here to find the best model representation, but rather point out additional difficulties brought up by the presence of large-scale superfluid motion.

The wall-normal profiles of the dimensionless  $\mathcal{P}^\dagger = \mathcal{P}_K / (V_{ns}^0)^2$  contributions to the production term are shown in Fig. 25. The main contribution  $\mathcal{P}_1$ , shown by purple dotted lines, is peaking in the channel core, where it is almost constant, then quickly decreasing toward the walls. This behavior is very similar to  $I_{\ell,x}(y)$  at all studied temperatures, with differences in the near-wall behavior. For the parabolic  $V_n$  profiles, Figs. 25(a)–25(c), at high temperature,  $\mathcal{P}_1$  remains nonzero even very close to the walls, at intermediate  $T = 1.65$  K  $\mathcal{P}_1$  drops to zero at about intervortex distance from the wall, while at low  $T$  it becomes negligible already at about  $2\ell$  from the nearest wall. Two other contributions,  $\mathcal{P}_2$  and  $\mathcal{P}_3$  are negligible compared to  $\mathcal{P}_1$  in the channel core, gradually increasing toward the walls and attaining the largest values at the distance  $\ell$  from them. Here we see the largest

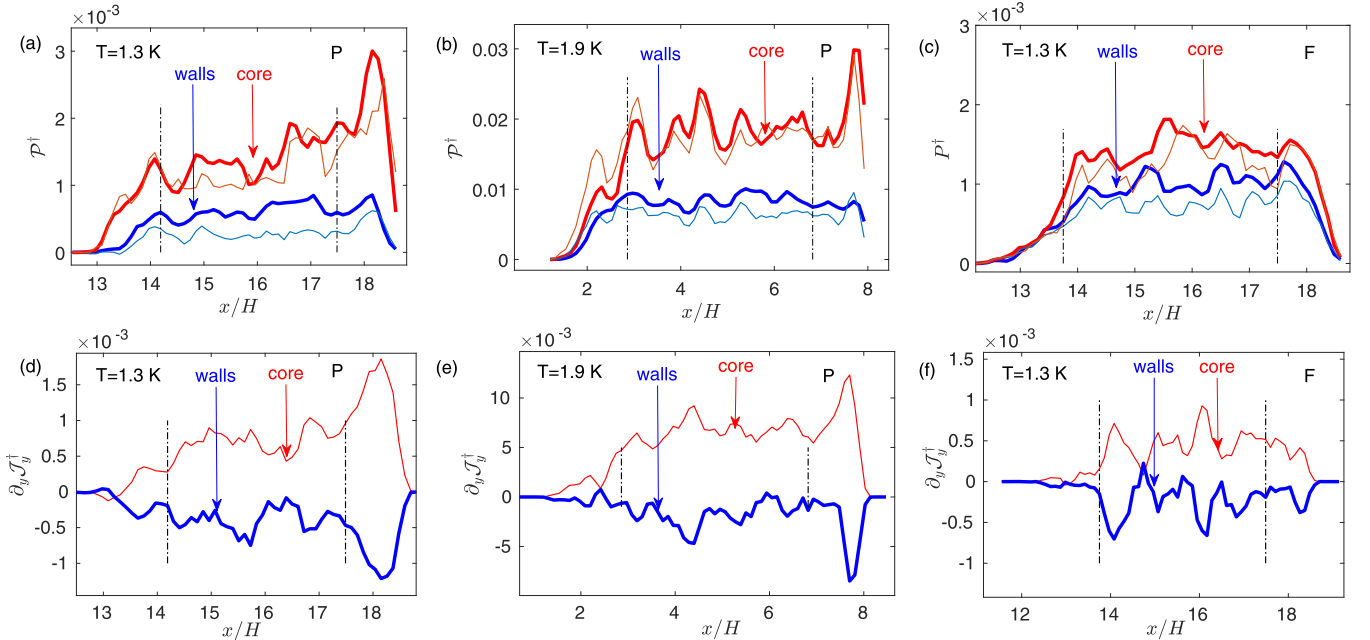


FIG. 26. [(a)–(c)] The streamwise profiles of the production terms:  $\mathcal{P}_1$  [Eq. (12), thin lines], and the total production  $\mathcal{P}_1 + \mathcal{P}_2 + \mathcal{P}_3$  (thick lines) for different conditions. (a)  $T = 1.3$  K, parabolic  $V_n$  with  $U_c = 3$  cm/s; (b)  $T = 1.9$  K, parabolic  $V_n$  with  $U_c = 1$  cm/s; and (c)  $T = 1.3$  K, flattened  $V_n$  profile. [(d)–(f)] The streamwise profiles of  $\partial \mathcal{J}_y / \partial y$ . To calculate the derivative, at each  $x$ -point  $\mathcal{J}_y(y)$  was fitted by seventh-degree polynomial function. The resulting  $\partial \mathcal{J}_y(x, y) / \partial y$  was averaged over the core and the near-wall regions. The profiles  $\partial \mathcal{J}_y^{\text{wall}} / \partial y$  are the sum over both near-wall regions. Thin dot-dashed black lines mark the edges of the bulk region.

difference between the high and low  $T$  behavior. At  $T = 1.9$  K, the contributions of  $\mathcal{P}_2$  and  $\mathcal{P}_3$  may be safely neglected everywhere in the channel. At  $T = 1.65$  K, the contribution of  $\mathcal{P}_2$  becomes important, while at  $T = 1.3$  K, both  $\mathcal{P}_2$  and  $\mathcal{P}_3$  are dominant near the walls, such that overall production in this region is about half of that in the channel core. As a result, the total production wall-normal profile becomes similar to that for the flattened  $V_n$  profile at this temperature, Fig. 25(d), although in the latter case  $\mathcal{P}_1$  has the dominant contribution (about 90%) everywhere in the channel. For this type of the  $V_n$  profile, the contributions of  $\mathcal{P}_2$  and  $\mathcal{P}_3$  may be neglected at all temperatures, especially at high  $T$ . The difference between the production in the channel core and in the near-wall regions is much smaller than for the parabolic  $V_n$  profiles. These features are even more pronounced at higher temperatures.

To see how the VLD production is distributed along the tangle, we plot in Figs. 26(a)–26(c) the streamwise profiles of  $\mathcal{P}_1^\dagger$  and of the total production  $\mathcal{P}_1^\dagger + \mathcal{P}_2^\dagger + \mathcal{P}_3^\dagger$  for the same conditions as in Fig. 25. We do not show the profiles for  $T = 1.65$  K, as they represent an intermediate case and do not bring more information.

First of all, we can clearly distinguish the bulk, the hot and the cold front regions. In the tangle bulk, the production is almost constant, up to fluctuations that are stronger

in the channel core than in the near-wall region. In accordance with profiles shown in Fig. 25, the contribution of  $\mathcal{P}_1$  (thin lines) is dominant at high  $T$ , Fig. 26(b), both in the core and near walls, as well as for the flows generated by the flattened  $V_n$  profiles, Fig. 26(c). At low  $T$ , Fig. 26(a),  $\mathcal{P}_1$  constitutes about half of the total production in the near-wall region.

In the hot front region, the production in the core has a pronounced peak in the channel core, very close to the tangle edge, which is dominated by  $\mathcal{P}_1$ . The VLD produced in this region is then taken to the walls by the transverse flux, as is well seen in Figs. 26(d)–26(f) where we plot  $\partial \mathcal{J}_y^\dagger(x)/\partial y$ , for the dimensionless  $\mathcal{J}_y^\dagger = \mathcal{J}_y \kappa / (V_{ns}^0)^2$ . Although this peak is not as pronounced in the flows generated by the flattened  $V_n$  profiles, the production is still stronger in the channel core than near the walls. The horseshoe shape of the VLD distribution, as in Fig. 10(c), is the result of this dominant production in the channel core and the outward flux in the hot front region.

The situation is completely different in the cold front region, where the production and the fluxes are strongly suppressed. Here, the production, the decay, and the fluxes balance each other in a manner that strongly depends on the flow conditions.

- 
- [1] R. J. Donnelly, *Quantized Vortices in Helium II* (Cambridge University Press, Cambridge, 1991).
- [2] *Quantized Vortex Dynamics and Superfluid Turbulence*, edited by C. F. Barenghi, R. J. Donnelly and W. F. Vinen (Springer-Verlag, Berlin, 2001), Vol. 571.
- [3] W. F. Vinen and J. J. Niemela, Quantum turbulence, *J. Low Temp. Phys.* **128**, 167 (2002).
- [4] S. K. Nemirovskii, Quantum turbulence: Theoretical and numerical problems, *Phys. Rep.* **524**, 85 (2013).
- [5] R. P. Feynman, Application of quantum mechanics to liquid helium, *Prog. Low Temp. Phys.* **1**, 17 (1955).
- [6] W. F. Vinen, Mutual friction in a heat current in liquid helium II I. Experiments on steady heat currents, *Proc. R. Soc.* **240**, 114 (1957); Mutual friction in a heat current in liquid helium II. II. Experiments on transient effects, **240**, 128 (1957); Mutual friction in a heat current in liquid helium II III. Theory of the mutual friction, **242**, 493 (1957); Mutual friction in a heat current in liquid helium. II. IV. Critical heat currents in wide channels, **243**, 400 (1958).
- [7] J. T. Tough, Superfluid turbulence, in *Progress in Low Temperature Physics*, edited by D. F. Brewer (North-Holland, Amsterdam, 1982), Vol. VIII, p. 133.
- [8] V. P. Peshkov and K. Tkachenko, Kinetics of destruction of superfluidity in Helium, *Sov. Phys. JETP* **14**, 1019 (1962).
- [9] V. K. Tkachenko, Development of turbulence, in the presence of a heat flow in Helium II within a capillary and the critical velocity problem, *Sov. Phys. JETP* **18**, 1251 (1964).
- [10] R. P. Slegtenhorst, G. Marees, and H. van Beelen, Transient effects in superfluid turbulence, *Physica B* **113**, 367 (1982).
- [11] K. W. Schwarz and J. R. Rozen, Transient behavior of superfluid turbulence in a large channel, *Phys. Rev. B* **44**, 7563 (1991).
- [12] D. D. Awschalom, F. P. Milliken, and K. W. Schwarz, Properties of Superfluid Turbulence in a Large Channel, *Phys. Rev. Lett.* **53**, 1372 (1984).
- [13] H. van Beelen, W. van Jooligen, and K. Yamada, On a balance equation for superfluid vorticity in capillary flow of helium II, *Physica B* **153**, 248 (1988).
- [14] S. K. Nemirovskii, W. Fiszdon, Chaotic quantized vortices and hydrodynamic processes in superfluid helium, *Rev. Mod. Phys.* **67**, 37 (1995).
- [15] S. K. Nemirovskii, Propagation of a turbulent fronts in quantum fluids, *J. Low Temp. Phys.* **162**, 347 (2011).
- [16] K. W. Schwarz, Three-dimensional vortex dynamics in superfluid  $^4\text{He}$ : Homogeneous superfluid turbulence, *Phys. Rev. B* **38**, 2398 (1988).
- [17] T. Lipniacki, Evolution of the line-length density and anisotropy of quantum tangle in  $^4\text{He}$ , *Phys. Rev. B* **64**, 214516 (2001).
- [18] D. Jou and M. S. Mongiovì, Description and evolution of anisotropy in superfluid vortex tangles with counterflow and rotation, *Phys. Rev. B* **74**, 054509 (2006).
- [19] D. Khomenko, V. S. L'vov, A. Pomyalov, and I. Procaccia, Dynamics of the vortex line density in superfluid counterflow turbulence, *Phys. Rev. B* **97**, 014508 (2018).
- [20] J. Castiglione, P. J. Murphy, J. T. Tough, and F. Hayot, Propagating and stationary superfluid turbulent fronts, *JLTP* **100**, 575 (1995).
- [21] K. W. Schwarz, Phase Slip and Turbulence in Superfluid He: A Vortex Mill that Works, *Phys. Rev. Lett.* **64**, 1130 (1990).
- [22] T. V. Chagovets, and S. W. Van Sciver, A study of thermal counterflow using particle tracking velocimetry, *Phys. Fluids* **23**, 107102 (2011).

- [23] M. La Mantia, Particle trajectories in thermal counterflow of superfluid helium in a wide channel of square cross section, *Phys. Fluids* **28**, 024102 (2016).
- [24] B. Mastracci and W. Guo, Exploration of thermal counterflow in He II using particle tracking velocimetry, *Phys. Rev. Fluids* **3**, 063304 (2018).
- [25] A. W. Baggaley and J. Laurie, Thermal Counterflow in a Periodic Channel with Solid Boundaries, *JLTP* **178**, 35 (2015).
- [26] A. W. Baggaley, and S. Laizet, Vortex line density in counterflowing He II with laminar and turbulent normal fluid velocity profiles, *Phys. Fluids* **25**, 115101 (2013).
- [27] S. Yui and M. Tsubota, Counterflow quantum turbulence of He-II in a square channel: Numerical analysis with nonuniform flows of the normal fluid, *Phys. Rev. B* **91**, 184504 (2015).
- [28] J. Gao, W. Guo, S. Yui, M. Tsubota, and W. F. Vinen, Dissipation in quantum turbulence in superfluid  $^4\text{He}$  above 1 K, *Phys. Rev. B* **97**, 184518 (2018).
- [29] D. Khomenko, L. Kondaurova, V. S. L'vov, P. Mishra, A. Pomyalov, and I. Procaccia, Dynamics of the density of quantized vortex lines in superfluid turbulence, *Phys. Rev. B* **91**, 180504(R) (2015).
- [30] D. Khomenko, V. S. L'vov, P. Mishra, A. Pomyalov, I. Procaccia, Reply to "Comment on 'Dynamics of the density of quantized vortex lines in superfluid turbulence'", *Phys. Rev. B* **94**, 146502 (2016).
- [31] S. K. Nemirovskii, Nonuniform quantum turbulence in superfluids, *Phys. Rev. B* **97**, 134511 (2018).
- [32] E. Varga, S. Babuin, V. S. L'vov, A. Pomyalov, and L. Skrbek, Transition to quantum turbulence and streamwise inhomogeneity of vortex tangle in thermal counterflow, *JLTP* **187**, 531 (2017).
- [33] H. Shan, B. Ma, Z. Zhang, and F. T. M. Nieuwstadt, Direct numerical simulation of a puff and a slug in transitional cylindrical pipe flow, *J. Fluid Mech.* **387**, 39 (1999).
- [34] M. Nishi, B. Ünsal, F. Durst, G. Biswas, Laminar-to-turbulent transition of pipe flows through puffs and slugs, *J. Fluid Mech.* **614**, 425 (2008).
- [35] D. Samanta, A. De Lozar, and B. Hof, Experimental investigation of laminar turbulent intermittency in pipe flow, *J. Fluid Mech.* **681**, 193 (2011).
- [36] D. Barkley, B. Song, V. Mukund, G. Lemoult, M. Avila, and B. Hof, The rise of fully turbulent flow, *Nature* **526**, 550 (2015).
- [37] B. Song, D. Barkley, B. Hof, and M. Avila, Speed and structure of turbulent fronts in pipe flow, *J. Fluid Mech.* **813**, 1045 (2017).
- [38] R. J. Donnelly, C. F. Barenghi, The Observed Properties of Liquid Helium at the Saturated Vapor Pressure, *J. Phys. Chem. Ref. Data* **27**, 1217 (1998).
- [39] L. Kondaurova, V. S. L'vov, A. Pomyalov, and I. Procaccia, Structure of a quantum vortex tangle in  $^4\text{He}$  counterflow turbulence, *Phys. Rev. B* **89**, 014502 (2014).
- [40] D. C. Samuels, Velocity matching and Poiseuille pipe flow in superfluid helium, *Phys. Rev. B* **46**, 11714 (1992).
- [41] A. Marakov, J. Gao, W. Guo, S. W. Van Sciver, G. G. Ihas, D. N. McKinsey, and W. F. Vinen, Visualization of the normal-fluid turbulence in counterflowing superfluid  $^4\text{He}$ , *Phys. Rev. B* **91**, 094503 (2015).
- [42] D. Khomenko, P. Mishra, A. Pomyalov, Coupled dynamics for superfluid  $^4\text{He}$  in the channel, *JLTP* **187**, 405 (2017).
- [43] S. Yui, M. Tsubota, and H. Kobayashi, Three-Dimensional Coupled Dynamics of the Two-Fluid Model in Superfluid  $^4\text{He}$ : Deformed Velocity Profile of Normal Fluid in Thermal Counterflow, *Phys. Rev. Lett.* **120**, 155301 (2018).
- [44] E. Varga and L. Skrbek, Dynamics of the density of quantized vortex lines in counterflow turbulence: Experimental investigation, *Phys. Rev. B* **97**, 064507 (2018).
- [45] A. N. Kolmogorov, I. Petrovskii, and N. Piskunov, A study of the diffusion equation with increase in the amount of substance and its application to a biology problem, in *Selected works of A. N. Kolmogorov*, edited by V. M. Tikhomirov (Kluwer Academic Publishers, London, 1991), Vol. I, p. 242; Original work *Bull. Univ. Moscow, Ser. Int. A* **1**, 1 (1937).
- [46] R. A. Fischer, The wave of advance of advantageous genes, *Proc. Annu. Symp. Eugen. Soc.* **7**, 355 (1937).
- [47] Y. B. Zel'dovich and D. A. Frank-Kamenetskii, A Theory of thermal propagation of flame, *Acta Physicochimica U. R. S. S.* **XVII**, 1–2, 42 (1938).
- [48] W. van Saarloos, Front propagation into unstable states: Marginal stability as a dynamical mechanism for velocity selection, *Phys. Rev. A* **37**, 211 (1988); Front propagation into unstable states. II. Linear versus nonlinear marginal stability and rate of convergence, **39**, 6367 (1989).
- [49] U. Ebert and W. van Saarloos, Front propagation into unstable states: universal algebraic convergence towards uniformly translating pulled fronts, *Physica D* **146**, 1 (2000).
- [50] M. Cencini, C. Lopez, and Davide Vergni, Reaction-diffusion systems: front propagation and spatial structures, *The Kolmogorov Legacy in Physics* (Springer, Verlag Berlin Heidelberg, 2003), Vol. 636, p. 196.
- [51] M. Abel, A. Celani, D. Vergni, and A. Vulpiani, Front propagation in laminar flows, *Phys. Rev. E* **64**, 046307 (2001).
- [52] S. Babuin, V. S. L'vov, A. Pomyalov, L. Skrbek, and E. Varga, Coexistence and interplay of quantum and classical turbulence in superfluid  $^4\text{He}$ , *Phys. Rev. B* **94**, 174504 (2016).
- [53] J. Gao, W. Guo, V. S. L'vov, A. Pomyalov, L. Skrbek, E. Varga, W. F. Vinen, The decay of counterflow turbulence in superfluid  $^4\text{He}$ , *JETP Lett.* **103**, 648 (2016).
- [54] S. K. Nemirovskii, Diffusion of inhomogeneous vortex tangle and decay of superfluid turbulence, *Phys. Rev. B* **81**, 064512 (2010).
- [55] W. Malfliet, Solitary wave solutions of nonlinear wave equations, *Am. J. Phys.* **60**, 650 (1992).
- [56] W. Malfliet, The tanh method: A tool for solving certain classes of nonlinear evolution and wave equations, *J. Comput. Appl. Math.* **164–165**, 529 (2004).
- [57] M. Tsubota, T. Araki, and W. F. Vinen, Diffusion of an inhomogeneous vortex tangle, *Physica B* **329–333**, 224 (2003).
- [58] E. Rickinson, N. G. Parker, A. W. Baggaley, and C. F. Barenghi, *Phys. Rev. A* **98**, 023608 (2018).
- [59] E. Rickinson, N. G. Parker, A. W. Baggaley, and C. F. Barenghi, Inviscid diffusion of vorticity in low-temperature superfluid helium, *Phys. Rev. B* **99**, 224501 (2019).